



1 **Airborne Lidar Observations of Wind, Water Vapor, and Aerosol Profiles During The**  
2 **NASA Aeolus Cal/Val Test Flight Campaign**

3  
4 Kristopher M. Bedka<sup>1</sup>, Amin R. Nehrir<sup>1</sup>, Michael Kavaya<sup>1</sup>, Rory Barton-Grimley<sup>1</sup>, Mark  
5 Beaubien<sup>6</sup>, Brian Carroll<sup>5</sup>, James Collins<sup>2</sup>, John Cooney<sup>5</sup>, G. David Emmitt<sup>3</sup>, Steven Greco<sup>3</sup>,  
6 Susan Kooi<sup>2</sup>, Tsengdar Lee<sup>4</sup>, Zhaoyan Liu<sup>1</sup>, Sharon Rodier<sup>2</sup>, Gail Skofronick-Jackson<sup>4</sup>

7  
8 <sup>1</sup>NASA Langley Research Center, Hampton, VA

9 <sup>2</sup>Science Systems and Applications, Inc., Hampton, VA

10 <sup>3</sup>Simpson Weather Associates, Charlottesville, VA

11 <sup>4</sup>NASA Headquarters, Washington D.C.

12 <sup>5</sup>NASA Postdoctoral Fellowship Program, Universities Space Research Association at NASA Langley Research  
13 Center, Hampton, VA

14 <sup>6</sup>Yankee Environmental Systems, Inc., Turners Falls, MA

15  
16 *Correspondence to:* Kristopher M. Bedka (kristopher.m.bedka@nasa.gov)

17  
18 **ABSTRACT**

19 Lidars are uniquely capable of collecting high precision and high spatio-temporal resolution observations that have  
20 been used for atmospheric process studies from the ground, aircraft, and space for many years. The Aeolus mission,  
21 the first space-borne Doppler wind lidar, was developed by the European Space Agency and launched in August 2018.  
22 Its novel Atmospheric LAsER Doppler INstrument (ALADIN) observes profiles of the component of the wind vector  
23 and aerosol/cloud optical properties along the instrument's line-of-sight (LOS) direction on a global scale. Two  
24 airborne lidar systems have been developed at NASA Langley Research Center in recent years that collect  
25 measurements in support of several NASA Earth Science Division focus areas. The coherent Doppler Aerosol WiNd  
26 (DAWN) lidar measures vertical profiles of LOS velocity along selected azimuth angles that are combined to derive  
27 profiles of horizontal wind speed and direction. The High Altitude Lidar Observatory (HALO) measures high  
28 resolution profiles of atmospheric water vapor (WV), and aerosol and cloud optical properties. Because there are  
29 limitations in terms of spatial and vertical detail and measurement precision that can be accomplished from space,  
30 airborne remote sensing observations like those from DAWN and HALO are required to fill these observational gaps  
31 as well as to calibrate and validate space-borne measurements.

32 Over a two-week period in April 2019 during their Aeolus Cal/Val Test Flight campaign, NASA conducted five  
33 research flights over the Eastern Pacific Ocean with the DC-8 aircraft. The purpose was to demonstrate: 1) DAWN  
34 and HALO measurement capabilities across a range of atmospheric conditions, 2) Aeolus Cal/Val flight strategies and  
35 comparisons of DAWN and HALO measurements with Aeolus to gain an initial perspective of Aeolus performance,  
36 and 3) how atmospheric dynamic processes can be resolved and better understood through simultaneous observations



37 of wind, WV, and aerosol profile observations, coupled with numerical model and other remote sensing observations.  
38 This paper provides a brief description of the DAWN and HALO instruments, discusses the synergistic observations  
39 collected across a wide range of atmospheric conditions sampled during the DC-8 flights, and gives a brief summary  
40 of the validation of DAWN, HALO, and Aeolus observations and comparisons.



41 **1. Introduction**

42 The Aeolus mission, the first-ever space-borne Doppler wind lidar (DWL), was developed by the European Space  
43 Agency (ESA) and launched in August 2018. Aeolus has a sun-synchronous orbit at 320 km altitude (Kanitz et al.  
44 2019), and carries a single payload, the Atmospheric LAsER Doppler INstrument (ALADIN). ALADIN observes  
45 profiles of the component of the wind vector along the instrument's line-of-sight (LOS) direction, on a global scale  
46 from the ground up to 30 km in the stratosphere (ESA 2016; Stoffelen et al. 2005; Reitebuch 2012; Kanitz et al. 2019).  
47 Aerosol optical properties are retrieved from ALADIN measurements employing an interferometric approach similar  
48 to the High Spectral Resolution Lidar (HSRL) technique (Shiple et al. 1983; Flamant et al. 2008). Aeolus observes  
49 horizontal wind speed and aerosol profiles along a single LOS. The Aeolus mission serves as both a technology  
50 demonstration as well as validation of predicted impacts of global wind profile observations on weather forecasting  
51 and atmospheric research. There is currently a robust international effort to conduct intensive Aeolus calibration and  
52 validation (Cal/Val) using ground and suborbital remote and in situ sensors as well as comparison against numerical  
53 model background fields (ESA 2019; Witschas et al. 2020; Lux et al. 2020; Baars et al. 2020; Martin et al. 2020;  
54 Khaykin et al. 2020). NASA's longstanding heritage in development and deployment of airborne DWL technologies,  
55 coupled with its interests in utilizing space-borne wind and aerosol observations for Earth system science process  
56 studies and weather prediction, served as the primary motivating factors for the agency to contribute to the Aeolus  
57 Cal/Val effort.

58 The 2017 Decadal Survey for Earth Science and Applications from Space (ESAS 2017) identified a set of  
59 key Earth science and applications questions to be addressed by the research community over the next decade. Two  
60 of these questions were related to 1) a better understanding planetary boundary layer (PBL) processes and air-surface  
61 fluxes and 2) an understanding of why clouds, convection, heavy precipitation, occur when and where they do.  
62 Measurements required to address these questions include aerosol vertical profiles and properties, PBL height, cloud  
63 type, depth and hydrometeor composition, temperature, water vapor and wind profiles, as well as many other  
64 geophysical variables. Observations of these variables are critical to numerical weather prediction models and  
65 reanalyses that have informed our understanding of the Earth's weather and climate system over the last 40+ years  
66 (Stith et al. 2018). A number of active and passive space-borne remote sensing systems collect such observations,  
67 however, they often lack horizontal and vertical resolution, spatial coverage, temporal frequency, and/or precision to  
68 enable detailed process studies and advance our understanding. ESAS (2017) recommends a future Earth System



69 Explorer class mission focusing on atmospheric wind measurement to address gaps in the current space-borne wind  
70 observing network. However, there are limitations as to how processes can be observed from space, thus ESAS (2017)  
71 also recommends airborne and ground based in-situ and remote sensing to fill observational gaps.

72 Lidars are uniquely capable of collecting high precision and high spatio-temporal resolution observations  
73 that have been used for atmospheric process studies from the ground, aircraft, and space for many years. Two airborne  
74 lidar systems have been developed at NASA Langley Research Center (LaRC) in recent years that collect  
75 measurements in support of the NASA Science Mission Directorate Earth Science Division Weather and Atmospheric  
76 Dynamics, Carbon Cycle, and Atmospheric Composition Science Focus Areas. Initially developed in the late 2000's,  
77 the Doppler Aerosol WiNd (DAWN, Kavaya et al. 2014) lidar measures vertical profiles of LOS velocity that are  
78 combined to derive horizontal wind speed and direction using the coherent detection method (see Henderson et al.  
79 2005 and references therein). More recently in 2015, the High Altitude Lidar Observatory (HALO), was developed to  
80 measure high resolution profiles of atmospheric water vapor (WV), aerosol/cloud optical properties. HALO also  
81 provides the option to substitute WV profile observations with a total column and mixed layer methane observation  
82 (Nehrir et al. 2018). The distribution of atmospheric WV and its coupling to circulation is a common focus across  
83 several of the World Climate Research Program (WCRP) Grand Challenges and progress requires improved  
84 understanding of processes based on “observations of WV, winds and clouds, especially in the lower troposphere, and  
85 at higher vertical resolution than is available from current sensors” (Asrar et al. 2015; Wulfmeyer et al. 2015; Nehrir  
86 et al. 2017; Stevens et al. 2017). Simultaneous, high spatio-temporal resolution (< 0.5 km vertical, 1-10 km spatial)  
87 wind, WV, and aerosol observations from DAWN and HALO serve as an ideal remote sensing payload for supporting  
88 a breadth of airborne science campaigns to address the key process-oriented science questions posed by the 2017  
89 Decadal Survey and WCRP, as well as for satellite Cal/Val activities such as for the Aeolus mission.

90 In April 2019, NASA conducted an Aeolus Cal/Val Test Flight campaign to demonstrate: 1) DAWN Doppler  
91 wind lidar and new HALO HRSL aerosol and WV DIAL observational capabilities across a range of atmospheric  
92 conditions, 2) flight strategies for Aeolus Cal/Val and comparisons with Aeolus to gain an initial perspective of Aeolus  
93 performance, in preparation for future international Aeolus Cal/Val airborne campaigns, and 3) how atmospheric  
94 dynamic processes can be resolved and better understood through simultaneous observations of wind, WV, and aerosol  
95 profile observations, coupled with numerical model and other remote sensing observations. Five NASA DC-8 aircraft  
96 flights were conducted over a period of two weeks over the Eastern Pacific and Southwest U.S., based out of NASA



97 Armstrong Flight Research Center in Palmdale, California and Kona, Hawaii. Dropsondes were used to validate the  
98 DAWN Aeolus wind observations and HALO WV observations. The LaRC Diode Laser Hygrometer (Diskin et al.  
99 2002) was also installed on the DC-8 and provided several in-situ WV validation profiles for both the HALO and  
100 dropsonde measurements.

101 This paper provides a brief description of the DAWN and HALO instruments, discusses the synergistic  
102 observations collected across a wide range of atmospheric conditions sampled during several DC-8 flights, and a  
103 summary of the validation of DAWN, HALO, and Aeolus observations and comparisons.

104

## 105 **2. Instrument Overview**

### 106 **2.1 DAWN**

107 DAWN, a pulsed 2-micron coherent-detection doppler wind lidar (DWL), was initially developed in the 2000's at  
108 NASA LaRC as an airborne instrument simulator to demonstrate technologies that would be required for a future  
109 space-borne doppler wind lidar mission as well as to support airborne process studies and satellite Cal/Val activities.  
110 DAWN is one of several airborne DWLs operated by the international community, such as those described by Wang  
111 et al. (2012), Witschas et al. (2017); Bucci et al. (2018), Lux et al. (2018), Marksteiner et al. (2018), Tucker et al.  
112 (2018), and Zhang et al. (2018).

113 An overview of the DAWN system architecture is described by Kavaya et al. (2014) and Greco et al. (2020),  
114 but a brief summary is provided here as background. During the 2019 Aeolus Cal/Val campaign, DAWN operated  
115 with a 10 Hz pulse repetition rate and 180 ns pulse duration, generating ~100 mJ per pulse. It originally generated 250  
116 mJ per pulse using a crystal amplifier for the GRIP and PolarWinds I and II campaigns described below. However,  
117 this component failed and the space it occupied was used for critical beam shaping optics that increased signal-to-  
118 noise ratio (SNR) significantly more than if the amplifier had been replaced. DAWN utilizes a 30° deflecting wedge  
119 scanner at the output of the system beam expander to enable vertical profiling of horizontal wind vectors. DAWN can  
120 scan at user-specified azimuth angles (commonly referred to as “looks”) with a user-specified number of laser pulse  
121 averages per LOS wind profile. Generally, a greater number of azimuths and pulses/azimuth improves vertical  
122 coverage of successful wind retrievals and cloud cover penetration, respectively, both at the expense of horizontal  
123 distance between profiles. DAWN also has the ability to stare at one azimuth angle to retrieve wind speed along the  
124 LOS which is analogous to Aeolus observations. Table 1 provides a summary of DAWN operating modes during the



125 campaign. The nominal operating mode is 5 azimuths ( $45^\circ$ ,  $22.5^\circ$ ,  $0^\circ$ ,  $-22.5^\circ$ ,  $-45^\circ$ ), with  $0^\circ$  oriented forward along  
126 flight track, and 20 pulses/azimuth, providing wind profiles every 4-5 km assuming nominal DC-8 cruise speeds of  
127 225-250 m/s and  $\sim 2$  seconds to move the scanner to a new azimuth.

128 DAWN wind retrievals are based on methods developed within the coherent DWL community, described by  
129 Kavaya et al. (2014) and Greco et al. (2020). The range-resolved retrieval is applied to each range gate spaced by 128  
130 samples corresponding to an along LOS range of  $\sim 38$  m at a 500 MHz sampling rate, which projects as 33 m in the  
131 vertical with a  $30^\circ$  off-nadir angle. For each retrieval, a range gate of 256 samples is zero padded to 1024 samples in  
132 the FFT spectral analysis to determine a Doppler shift in the received lidar signal. A 256 sample range gate computes  
133 to be 76 m along the LOS and 66 m in the vertical. The 180 ns DAWN pulse full width at half maximum (FWHM)  
134 yields a folded 27 m convoluted return along a LOS. With the  $30^\circ$  off nadir angle, that corresponds to a  $\sim 23$  m vertical  
135 return volume. In addition, the electronic bandwidth of 250 MHz yields an along LOS range of 0.6 m and a vertical  
136 range of 0.52 m. Therefore the current DAWN wind measurement has a minimum vertical range resolution of  $\sim 90$  m,  
137 but wind retrievals in each profile are spaced by 33 m in the vertical thus there is some correlation between adjacent  
138 vertical levels. FFT periodograms are averaged across the number of pulses per azimuth, with corrections employed  
139 to account for slight shot-to-shot shifts in transmitted laser frequency across the number of pulses. This shot  
140 accumulation improves SNR and thus permits wind measurements to have a higher success rate in lower  
141 concentrations of aerosols. The frequency shift is combined with aircraft airspeed and attitude information from the  
142 DC-8 INS/GPS system to derive a wind speed range profile along the LOS. Winds from multiple LOS are combined  
143 within a solver of a linear system of equations to derive a wind vector. In practice, the vertical wind is assumed zero  
144 to reduce the degrees of freedom.

145 If a successful wind retrieval could not be derived at the highest vertical resolution (a slant range of 76.7  
146 meters) due to low aerosol concentration, data is integrated in the vertical over increasingly deep layers of 153.4,  
147 306.8, 613.6, 1227.3 meters along each line of sight until a sufficient signal magnitude at least 1.5 times the standard  
148 deviation of the periodogram's noise floor power is achieved. This approach is similar to the Adaptive Sample  
149 Integration Algorithm (ASIA) described by Greco et al. (2020). However, unlike Greco et al. (2020) where a wind is  
150 retrieved from samples of each LOS at the same slant range possibly corresponding to different altitudes especially  
151 during the aircraft turns and ascent/descent, a DAWN wind retrieval is performed using samples of each LOS at the  
152 same altitude. This can improve wind retrievals during aircraft maneuvers. Figures 3b and 10d shows that most winds



153 are retrieved via multi-pulse integration at a single range bin (purple), analogous to the “base” retrievals described by  
154 Greco et al. (2020), but lower aerosol backscatter at middle levels (~2-5 km altitude) of the profile in the free  
155 troposphere required more vertical integration to achieve sufficient signal.

156 DAWN has been used for a variety of NASA studies over the last decade. DAWN first flew on the DC-8  
157 during the 2010 NASA Genesis and Rapid Intensification Processes (GRIP) campaign (Braun et al. 2013; Kavaya et  
158 al. 2014). DAWN was also operated from the ground to explore opportunities for wind energy applications offshore  
159 of Virginia (Koch et al. 2012). Additionally, DAWN participated in two flight campaigns, PolarWinds I and II, in  
160 2014 with the NASA UC-12B, and 2015 with the DC-8, respectively. PolarWinds II (Marksteiner et al. 2018) involved  
161 collaboration with the European Space Agency and the Deutsches Zentrum für Luft- und Raumfahrt (DLR). The  
162 NASA DC-8 and the DLR Falcon-20 exercised coordinated flight strategies during PolarWinds II that helped to inform  
163 the 2019 Cal/Val campaign strategy as well as future campaigns. During PolarWinds II, DAWN provided the first  
164 airborne DWL observations of a mesoscale barrier jet, driven by the interaction of synoptic scale wind with the steep  
165 and complex topography of Greenland (DuVivier et al. 2017). DAWN also flew aboard the DC-8 during the 2017  
166 Convective Processes Experiment (CPEX), a campaign which sought to better understand convective cloud dynamics,  
167 downdrafts, cold pools and thermodynamics during initiation, growth, and dissipation, as well as to improve model  
168 representation of convective and boundary layer processes through assimilation of DAWN and other remote sensing  
169 and in-situ observations (NASA 2017). DAWN wind profiles agreed very well with 169 dropsonde profiles in a  
170 variety of cloud, wind, and aerosol conditions, with less than 0.2 m/s bias (or “accuracy”) and 1.6 m/s root-mean-  
171 squared difference (RMSD, or “precision”) for wind components (Greco et al. 2020). DAWN wind observations were  
172 also well-correlated with flight-level winds measured in-situ by the DC-8 and near-surface wind measured by buoys.  
173 CPEX DAWN data were assimilated into a mesoscale model to improve simulations of a mesoscale convective system  
174 and tropical storm (Cui et al. 2020) and used to demonstrate how airborne radar and Doppler wind lidar data can be  
175 used together to study convective processes (Turk et al. 2020).

176 A 2-micron coherent detection Doppler wind lidar has been used by DLR for almost 20 years within a variety  
177 of airborne science campaigns. Witschas et al. (2020) describes that detailed comparisons between the DLR lidar and  
178 sonde demonstrate a bias of this system to be  $< 0.10$  m/s and a scaled median absolute deviation (approximately the  
179 same as RMSD due to minimal bias) between 0.9 and 1.5 m/s. This level of performance was deemed suitable for  
180 Aeolus Cal/Val during the DLR WindVal III and Aeolus Validation Through Airborne Lidars in Europe (AVATARE)



181 campaigns. Though the DLR pulse energy, pulse length, and spatial sampling interval differs from DAWN, the  
182 DAWN has provided similar performance to the DLR system in previous campaigns, and therefore is also a useful  
183 benchmark for validating Aeolus wind profiles.

184 Throughout the 2019 Aeolus campaign, the DAWN INS/GPS unit operated unreliably. This unit was  
185 designed to collect data at 10 Hz that could be synced with each DAWN laser pulse to remove aircraft speed and  
186 attitude effects from the returned atmospheric signal for retrieval of Doppler shift caused by aerosol motions, as  
187 described by Greco et al. (2020). The DC-8 1 Hz INS/GPS data was interpolated to the time of each DAWN pulse  
188 and used in place of the DAWN 10 Hz unit. Based on periods where there were reliable 10 Hz INS/GPS data, we  
189 found that use of 1 Hz data does add some variance to the DAWN wind retrieval, ranging from ~0.1-0.3 m/s and 0.5°-  
190 2.5° degrees in wind speed and direction, respectively based on sensitivity analyses. Attempts to address issues with  
191 the problematic INS/GPS unit resulted in periods generally less than 10 min of DAWN lidar downtime at various  
192 times during the flights.

193

## 194 **2.2 HALO**

195 NASA Langley Research Center developed HALO to address the observational needs of NASA Earth Science  
196 Division Weather and Atmospheric Dynamics, Carbon Cycle, and Atmospheric Composition Science Focus Areas.  
197 HALO is a modular and multi-function airborne lidar developed to measure atmospheric H<sub>2</sub>O and CH<sub>4</sub> mixing ratios  
198 and aerosol, cloud, and ocean optical properties using the differential absorption lidar (DIAL, Measures 1984, Nehrir  
199 et al. 2017) and high spectral resolution lidar (HSRL, Hair et al. 2008) techniques, respectively. HALO was designed  
200 as a compact replacement for the LASE WV DIAL (Browell et al. 1997) with improved and substantial additional  
201 capabilities (Nehrir et al. 2017-19). Furthermore, HALO was designed as an airborne simulator for future space-borne  
202 greenhouse gas DIAL missions called for by ESAS (2017) and also serves as testbed for risk reduction of key  
203 technologies required to enable those future space-borne missions. To respond to a wide range of airborne process  
204 studies, HALO can be rapidly reconfigured to provide either, H<sub>2</sub>O DIAL/HSRL, CH<sub>4</sub> DIAL/HSRL, or CH<sub>4</sub> DIAL/H<sub>2</sub>O  
205 DIAL measurements using three different modular laser transmitters and a single multi-channel and multi-wavelength  
206 receiver. Though HALO has successfully flown in several field campaigns in the CH<sub>4</sub> DIAL/HSRL configuration, the  
207 2019 Aeolus Cal/Val campaign was the maiden deployment for the H<sub>2</sub>O DIAL/HSRL configuration. Despite serving



208 as the first set of engineering test flights, HALO exceeded all expectations during the Aeolus Cal/Val campaign,  
209 demonstrating the first new airborne WV DIAL capability within NASA in over 25 years.

210 In the H<sub>2</sub>O DIAL/HSRL configuration, HALO employs a 1 KHz pulse repetition frequency injection seeded,  
211 Nd:YAG pumped optical parametric oscillator (OPO) pulsed laser to enable WV profile measurements at 935 nm  
212 using the DIAL technique, as well as the HSRL technique at 532 nm to make independent, unambiguous retrievals of  
213 aerosol extinction and backscatter. It also employs the standard backscatter technique at 1064 nm and is polarization-  
214 sensitive at the 1064/532 nm wavelengths. To enable WV profiling over a large dynamic range throughout the  
215 troposphere, HALO transmits four discrete wavelengths (three wavelength pairs) at 935 nm positioned on and off  
216 varying strength WV absorption lines where each transmitted wavelength pair provides sensitivity to a different part  
217 of the atmosphere. The profiles retrieved from the three transmitted line pairs are spliced together using a weighted  
218 mean where the WV optical depth is used to constrain the upper and lower bounds of the splice region. This WV  
219 sampling approach is similar to that presented by Wirth et al. (2009), however, HALO utilizes a single laser transmitter  
220 to generate all four transmitted wavelengths thereby significantly reducing the overall size, weight and power of the  
221 instrument. An overview paper summarizing the description and performance of HALO and its associated H<sub>2</sub>O, CH<sub>4</sub>,  
222 and HSRL measurements is currently in preparation.

223 HALO data are sampled at 0.5 s temporal and 1.25 m vertical resolution, respectively. Real-time onboard  
224 processing is employed to sum 125 shots at each of the four WV DIAL wavelengths and 500 shots at the 532 nm and  
225 1064 nm wavelengths to reduce the reported data rate to 2 Hz. A high sampling rate of 120 MHz is employed to allow  
226 for accurate CH<sub>4</sub> retrievals in the other HALO measurements configurations, as well as future cloud and ocean  
227 profiling. The WV DIAL and 1064 nm backscatter channels have an electrical bandwidth equivalent to 15 m vertical  
228 resolution. The electrical bandwidth for the HSRL channel at 532 nm is matched to the native sampling rate to achieve  
229 1.25 m vertical resolution in the atmosphere. The 532 nm signals are subsequently filtered and binned to 15 m vertical  
230 resolution in post-processing to increase the SNR of the HSRL aerosol retrievals.

231 The DIAL technique directly measures the molecular number density of water vapor. Conversion to mass or  
232 volume mixing ratio requires knowledge of the dry air number density which is obtained from MERRA-2 reanalysis  
233 fields of atmospheric pressure and temperature (Gelaro et al. 2017) that are interpolated in space and time to the lidar  
234 sampling track and resolution. The HALO water vapor mixing ratio (WVMR) products are averaged over 30-60  
235 seconds horizontally (6-12 km from the DC-8 assuming nominal cruise speed) and 315-585 m vertically to achieve



236 an absolute precision of better than 10% which are calculated using DIAL error propagation and Poisson photon  
237 statistics. The temporal and vertical averaging can be traded for precision in post processing and optimized for specific  
238 science applications. For the Aeolus Cal/Val campaign, HALO was able to demonstrate a precision of better than  
239 10% with 6 km along track averaging when the water vapor differential absorption optical depth (DAOD) was  
240 optimized through wavelength tuning for the viewing scene. Given that this campaign served as the first check flights  
241 for HALO, optimization of the WV DAOD within the lower troposphere was not achieved for parts of the first flight  
242 as well as the tropical scenes, resulting in loss of precision near the surface where the absorption was too large. For  
243 ease of interpretation across the various flights presented below, all of the HALO WV data are shown at a 12 km fixed  
244 horizontal resolution. To overcome the loss in precision for cases where the near surface DAOD was too large or  
245 SNR was degraded due to cloud attenuation, an adaptive vertical averaging routine is employed where the vertical  
246 resolution is increased from 315 m to 585 m when the uncertainty in the calculated WVMR drops below 10%. A  
247 weighted mean is used to transition between the two different vertical averaging bin sizes. The trades on HALO WV  
248 precision vs vertical and horizontal resolution as well as the adaptive vertical averaging routine will be the subject of  
249 a future paper.

250 Dropsonde humidity measurements during the Aeolus Cal/Val campaign lacked the vertical resolution and  
251 precision to validate the HALO WVMR retrievals, as is discussed in the following section. Qualitative comparisons,  
252 however, generally showed good agreement in the lower troposphere and into the PBL. Comparisons with the DLH  
253 in-situ open path measurement conducted during a spiral showed excellent agreement and are discussed further in  
254 Section 4.4. A detailed assessment of the HALO WV retrievals is beyond the scope of this paper and will be presented  
255 in a separate manuscript where statistical comparisons against the dropsondes, DLH in-situ measurements and satellite  
256 retrievals of the same geophysical variable will be discussed.

257 In addition to profiling WVMR throughout the troposphere, total or partial columns of precipitable WV are  
258 obtained by vertical integration of the WVMR profiles. WV profile data above the surface are limited to  
259 approximately the vertical resolution of the retrieval bin width which is required to achieve sufficient on/off extinction  
260 for high precision measurements. WV profiles over the ocean are extended to the surface utilizing the strong surface  
261 echo where a DIAL retrieval is carried out between the last good atmospheric retrieval above the surface and the on/off  
262 absorption from the surface echo. Preliminary results using the ocean surface echo show promise for extending the  
263 WV profile to the surface and compare favorably with in situ observations. Variability in surface height confounds



264 the surface return retrievals and are not employed over land for this study. Additionally, WV profiles above clouds  
265 are masked with an additional 45 m to avoid cloud edge effects and contamination in the DIAL retrieval.

266 One of the primary functions of HALO during the Aeolus Cal/Val campaign was to provide aerosol validation  
267 for the ALADIN co-polar aerosol backscatter and extinction products. The HALO aerosol HSRL and backscatter  
268 retrievals follow the methods presented by Hair et al. (2008). HALO aerosol backscatter and depolarization products  
269 are averaged 10 s horizontally and aerosol extinction products are averaged 60 s horizontally and 150 m vertically.  
270 The polarization and HSRL gain ratios are calculated as described in Hair et al. (2008). Operational retrievals also  
271 provide mixing ratio of non-spherical-to-spherical backscatter (Sugimoto and Lee 2006), distributions of aerosol  
272 mixed-layer height (MLH, Scarino et al., 2014), and aerosol type (Burton et al., 2012). Comparisons between HALO  
273 and Aeolus Level 2A atmospheric optical properties products during this Aeolus Cal/Val campaign are not presented  
274 here due to current limitations of Aeolus aerosol/cloud discrimination and low sensitivity to aerosol scattering  
275 throughout the troposphere. A comprehensive assessment between the Aeolus and HALO HSRL retrievals will be  
276 carried upon the next public release of the Aeolus L2A optical properties product, which is expected in the first quarter  
277 of 2021..

278

### 279 **2.3 Dropsondes**

280 The Yankee Environmental Systems, Inc. High-Definition Sounding System (HDSS) is an automated system  
281 deploying the expendable digital dropsonde (XDD) designed to measure wind and pressure–temperature–humidity  
282 (PTH) profiles, and skin sea surface temperature. A full technical description of the HDSS and XDD (referred to as  
283 sonde hereafter) systems is provided by Black et al. (2017). HDSS XDD sonde data were used during the 2015 Polar  
284 Winds II campaign and 2017 CPEX campaigns to validate DAWN as well as the 2015 Office of Naval Research  
285 Tropical Cyclone Intensity (TCI) field program to study the horizontal structure of tropical cyclones (Doyle et al.  
286 2017). The sonde measures PTH profiles at 2-Hz rate and GPS location, altitude and horizontal wind velocity at 4-  
287 Hz, equating to 5-8 meters per vertical level. During the Aeolus campaign, a new RH sensor deployed for the first  
288 time within the sonde was found to have lag in response and did not have adequate sensitivity to vertical water vapor  
289 (WV) gradients. An initial view of this is provided by Figure 14a above 5 km altitude, which will be further discussed  
290 in Section 4. Due to this response lag, sonde WV profiles will not be discussed in detail in this paper.



291 A set of processing steps and filters are applied to ensure sonde data quality and that the two datasets are of  
292 comparable vertical resolution. The sonde wind data are first smoothed using a running 3 vertical level boxcar average  
293 to minimize noise. Sonde wind data in the first 250 m beneath the aircraft were found to be artificially fast due to the  
294 sonde being recently released from the aircraft, so all measurements taken within the first 250 m are removed from  
295 any analysis. One sonde, released at 28 April at 0202 UTC, is especially noisy above 8 km so only sonde and DAWN  
296 data below 8 km are compared for that time. In addition, the sonde altitude is adjusted by adding 40 m to each sonde  
297 altitude measurement in order to account for a timing lag between when the sonde measurement is collected and the  
298 time stamp of a given vertical level as suggested by M. Beaubien (personal communication). Sonde wind data within  
299 +/- 33 m of each DAWN altitude bin are averaged, given that the DAWN pulse length projected into the vertical is  
300 approximately 23 m. The DAWN wind profile immediately preceding a sonde launch was used for comparison,  
301 provided that the profile occurred within 2.5 minutes of the sonde release to minimize the impact of spatial wind  
302 variability on the validation statistics. DAWN data met this time match criteria for 61 of the 65 sondes released across  
303 the five flights. Wind speed (direction) differences exceeding  $10 \text{ m s}^{-1}$  ( $30^\circ$ ) were considered outliers that amounted  
304 to 0.03% (3.57%) of 12,284 DAWN vertical bins matched with sonde data.

305

#### 306 **2.4 Aeolus**

307 Aeolus is a direct detection Doppler wind lidar operating near 355 nm that retrieves wind speed and aerosol and cloud  
308 profiles along a single LOS oriented  $90^\circ$  to the right of the Aeolus spacecraft heading (Straume et al. 2019; Kanitz et  
309 al. 2019; Reitebuch et al. 2019 and references therein). Aeolus derives wind profiles by measuring the Doppler shift  
310 of light backscattered from molecules (Rayleigh scattering), or clear sky aerosol and cloud particles (Mie scattering).  
311 In this study, we analyze the Aeolus Level 2B horizontally projected LOS (HLOS) wind speed product that is  
312 developed by the Royal Dutch Meteorological Institute (KNMI) and the European Centre for Medium-Range Weather  
313 Forecasts (ECMWF) under ESA contract, in close cooperation with teams developing the L1B product (DLR, DoRIT)  
314 and L2A product (Météo-France). Technical descriptions of the Aeolus wind retrieval processing and the Level 2B  
315 product are summarized by Tan et al. (2008); Rennie et al. (2018), Witschas et al. (2020) and references therein.

316 The DC-8 flew along the Aeolus track for 45 to 110 minutes, flight dependent, and was along the Aeolus  
317 track when the satellite was overhead, resulting in little spatial and temporal variability between the observations. The  
318 evening overpass near 6 PM local time was the target for all five underflights. The Aeolus laser LOS coordinates at a



319 6 km altitude were used to develop the DC-8 flight track. The DC-8 flew over a range of altitudes during the Aeolus  
320 underpasses, from 7.5 to 12 km depending on the atmospheric conditions and the specific objectives of a given flight.

321 Aeolus Level 2B products provide Mie winds at 10 km intervals where clouds are present and 0.5-1.0 km  
322 vertical spacing, and Rayleigh clear winds at near 90 km intervals and 1 km vertical spacing at altitudes sampled by  
323 DAWN, and up to 2 km in the lower stratosphere. When DAWN was in vector wind profiling mode, DAWN vector  
324 winds were projected to the Aeolus viewing orientation to derive a LOS wind speed. During the Aeolus underpass on  
325 the first flight of the campaign (17-18 April 2019, see Table 1), DAWN was mostly operated in single LOS mode with  
326 its beam oriented 90° to the right of the aircraft heading in order to match the sampling of Aeolus. DAWN data are  
327 averaged to match the Aeolus horizontal and vertical bin spacing and DAWN outliers in each bin are filtered from the  
328 averaging. At least 30 (10) valid DAWN wind retrievals must be present within a Rayleigh clear (Mie cloudy) bin to  
329 derive a robust mean for Aeolus comparison. We used the “estimated HLOS error” parameter provided in the Aeolus  
330 Level 2B product, where it is recommended that Rayleigh clear (Mie cloudy) winds with  $> 8$  m/s ( $> 5$  m/s) be excluded  
331 (Rennie and Isaksen 2020). An DAWN-Aeolus difference exceeding 20 m/s, which only occurred in one bin, was  
332 considered an outlier and excluded from analysis. These criteria and the duration of the Aeolus underpasses resulted  
333 in 231 vertical Rayleigh Clear and 42 Mie Cloudy data bins distributed across 46 Aeolus Rayleigh profiles.

334 It is important to note that, due to a variety of technical challenges that are beyond the scope of this paper,  
335 the Aeolus Laser-A output power gradually decreased from the time of Aeolus launch to April 2019 when the Aeolus  
336 Cal/Val Test Flight campaign was conducted (Lux et al. 2020). This degradation coupled with lower than expected  
337 signal throughput in detection chain (both of which are currently being studied by the Aeolus team), served to 1)  
338 decrease the precision of Aeolus Rayleigh and Mie derived wind products and 2) limit the ability to retrieve aerosol  
339 products from the Mie channel under clean or very tenuous aerosol loading conditions. ESA made the decision to  
340 switch to Aeolus Laser-B in June 2019, which has resulted in improved laser energy output and hence improved  
341 precision in the wind products. In addition, anomalous signal detections have been found on the Aeolus Aeolus  
342 Charged Coupled Device (ACCD) have been discovered (i.e. “hot pixels”) and the number of affected pixels have  
343 increased over time. A dedicated dark current calibration mode (DUDE) and an on-ground correction scheme based  
344 on the DUDE measurements has been implemented in the ground segment in June 2019, hence has not been applied  
345 to the measurements validated here.



346 Finally, comparisons of the Aeolus data quality with the ECMWF model background and collocated  
347 CAL/VAL observations from ground-based instrumentation (including wind profilers and radiosondes) showed that  
348 the variability of the Earth top-of-atmosphere total radiance along the Aeolus orbit cause thermal stress an  
349 deformations of the instrument telescope which could not be fully compensated by the implemented telescope thermal  
350 control. This has caused biases of the Aeolus L2B winds of several m/s varying along the orbit and from orbit to orbit  
351 (Martin et al. 2020). An on-ground correction of the telescope temperature induced bias has been developed and was  
352 implemented in April 2020. The dataset used in this comparison is hence affected by this known bias contributor.

353 The presented work includes preliminary data (not fully calibrated/validated and not yet publicly released)  
354 of the Aeolus mission that is part of the ESA Earth Explorer Programme. This includes wind products from before the  
355 public data release in May 2020 and/or aerosol and cloud products, which have not yet been publicly released. The  
356 preliminary Aeolus wind products will be reprocessed during 2020 and 2021, which will include in particular a  
357 significant L2B product wind bias reduction and improved L2A radiometric calibration. Aerosol, cloud, and wind  
358 products from the April 2019 period will become publicly available by fall 2021. The processor development,  
359 improvement and product reprocessing preparation are performed by the Aeolus DISC (Data, Innovation and Science  
360 Cluster), which involves government and industry partners including DLR, DoRIT, ECMWF, KNMI, CNRS, S&T,  
361 ABB and Serco, in close cooperation with the Aeolus PDGS (Payload Data Ground Segment). It is likely that  
362 performance will improve with future reprocessing, thus extensive validation of these preliminary products will not  
363 be emphasized in this paper.

364

### 365 **3. Flight Campaign Operations Description**

366 Five DC-8 flights were executed from 17-30 April 2019, four from NASA Armstrong Flight Research Center in  
367 Palmdale, California, and one from Kona, Hawaii along flight tracks overlaid on GOES-17 imagery shown in Figure  
368 1. Given the short duration of this campaign and other operational considerations, we generally sought to maximize  
369 the weather targets of opportunity, with an emphasis on broad regional sampling rather than focused sampling of one  
370 particular area or phenomenon. An exception to this was the 29-30 April flight where we transected the same regions  
371 multiple times to study atmospheric temporal variability and instrument performance. Flight tracks were selected to  
372 capture a diversity of wind and WV conditions while avoiding optically thick mid- to upper-level cloud layers that  
373 can attenuate lidar signals and inhibit vertical profiling throughout the troposphere. GOES-17 satellite imagery and



374 NASA Global Modeling and Assimilation Office (GMAO) Goddard Earth Observing System, Version 5 (GEOS-5)  
375 model forecasts of clouds, precipitation, and aerosols were used as guidance for flight planning.

376 GOES-17 visible and infrared satellite imagery was uploaded in near-real time to the DC-8, where it could  
377 be displayed and animated during flight for situational awareness and to help identify clear or broken cloud conditions  
378 for sonde releases. A GOES-17 Advanced Baseline Imager (ABI) Mesoscale Domain Sector (MDS) was provided by  
379 NOAA's National Environmental Satellite, Data, and Information Service (NESDIS) along the DC-8 flight track  
380 during almost the entirety of the 46-hour flight campaign. Images were collected every minute within an MDS, which  
381 enable a variety of cloud process and geostationary cloud- and WV-tracked atmospheric motion vector studies that  
382 are currently being conducted. Several examples of GOES-17 7.3  $\mu\text{m}$  WV channel imagery are shown below. This  
383 channel typically senses upwelling radiance emitted within the 500-750 hPa layer (~3 to 6 km altitude) in cloud-free  
384 conditions, a layer that was observed during all flights.

385

#### 386 **4. Results and Validation**

##### 387 **4.1 17-18 April 2019**

388 The first flight of the campaign served as both a test flight to ensure that all instrumentation and components were  
389 operating properly, as well as a science flight. The target of the flight was a strong mid-latitude cyclone over the  
390 North Pacific, centered at 51° N, 140° W and shown in Figure 2a-b. The goal was to intersect the large dry slot (Figure  
391 2d) of the cyclone where clear sky to broken cumulus clouds and wind speeds exceeding 50 m/s were present at flight  
392 level at the time of the Aeolus overpass near 03 UTC (27 UTC in the cross sections).

393 After system testing during the first three hours of the flight, DAWN was operated in three modes specified  
394 in Table 1. This flight was the only one to use a single LOS DAWN stare oriented 90° to the right of the aircraft  
395 heading, which emulated the view of Aeolus and produced higher spatial resolution profiles than operations with  
396 multiple LOS, ~0.5 km per single LOS speed profile vs 4-5 km per vector profile. During the stare periods, DAWN  
397 was periodically reset to operate in five azimuth vector profiling mode so that DAWN wind speed and direction could  
398 be validated with sondes being released in support of Aeolus validation. Due to the differences in DAWN operating  
399 mode throughout the flight, all DAWN vector wind profiles were projected to the LOS horizontal wind speed along  
400 the 90° azimuth. A time-height cross-section of DAWN and HALO data during the intensive observing period (IOP)  
401 on April 18 is shown in Figure 3. Figure 3a shows the absolute value of the DAWN LOS wind speed to account for



402 changing aircraft direction. As this was the first-ever flight of HALO in the WV profiling configuration, system  
403 testing persisted until approximately 03 UTC on 18 April.

404 The IOP for this flight began while the DC-8 was flying within a cold front with cirrus cloud at flight level  
405 and opaque mid- to low-level clouds beneath, which often obscured DAWN and HALO measurements from reaching  
406 the surface. The DC-8 was already along the Aeolus flight track at this time (white arrow in Figure 1a). After  
407 progressing through the frontal region, a dropsonde was released at 02.58 (0236) UTC while DAWN was briefly reset  
408 to vector wind profiling mode (Figure 4a). The DAWN, and to a lesser extent, MERRA-2 wind profile agreed with  
409 the sonde. LOS wind speed near flight level continued to increase until a local maximum just before 0300 UTC at the  
410 time of the Aeolus overpass at 0258 UTC. Two sonde releases were coordinated with DAWN vector profiles at ~02.83  
411 to 03.02 (0250-0301) UTC, again demonstrating excellent agreement between sonde and DAWN (Figures 4b-c).  
412 HALO aerosol backscatter (Figure 3c) depicted a prominent plume of elevated smoke (identified using HSRL aerosol  
413 intensive parameters, not shown) from approximately 2 km altitude that rose to 6 km as it was advected toward the  
414 low pressure center.

415 As the DC-8 approached opaque cumulus clouds close to the low center at 03.7 UTC, it turned southeastward  
416 along a long linear segment on the return to Palmdale. Opaque mid-level cloud cover associated with the front again  
417 inhibited profiling down to the surface, except for a few isolated profiles in breaks between clouds. While DAWN  
418 was reset at 05.5 UTC to address the problematic INS/GPS unit, a sharp transition into a high pressure region with  
419 weak wind flow occurred. Enhanced PBL moisture exceeding 10 g/kg near the surface was observed by HALO south  
420 of the front around 05.5 UTC (Figure 3d). A dropsonde was released at 0605 UTC, showing winds less than 5 m/s  
421 throughout much of the profile that were captured well by DAWN and MERRA-2 (Figure 4d), demonstrating that  
422 DAWN can accurately measure both high and very low wind speeds. Detailed comparisons between DAWN and  
423 MERRA-2 will be highlighted in a future paper.

424 Aerosol backscatter in this region was greater on average than the region near to the low pressure to the north  
425 with a prominent dust plume in the 2-4.5 km layer after 06.25 UTC (via aerosol intensive parameters, not shown)  
426 Between this dust and stratocumulus (stratocu hereafter) cloud layer below, an extremely dry layer was present which  
427 could have been driven by dehydration from radiative cooling and/or subsidence. Although serving primarily as a test  
428 flight, this first IOP provided insight into the performance of new synergistic lidar remote sensing capabilities critical  
429 for improved understanding of atmospheric processes.



430

431 **4.2 22-23 April 2019**

432 The second flight on 22-23 April focused on sustained higher altitude operations, targeting a high pressure region over  
433 the ocean where an Aeolus overpass was located near  $129.5^{\circ}$  W, followed by a low pressure region that extended  
434 through the depth of the troposphere, centered near the Arizona – Mexico border (Figure 5a-b). Between these two  
435 systems was a northeast-southwest oriented jet streak located across southern California and Nevada. This jet streak  
436 had winds over 90 kts (46.3 m/s) and can be seen via dry air in GOES-17  $7.3 \mu\text{m}$  imagery in Figure 1b, resulting from  
437 subsidence within a tropopause fold. The jet streak is evident in the DAWN wind speed cross-sections during the  
438 outbound and return legs of the Aeolus underflight at approximately 0.8 and 04.3 UTC, respectively (Figure 6a-b).  
439 DAWN observed over 40 m/s northerly winds above 10 km within the jet core, with winds over 20 m/s extending  
440 down to 5 km altitude. The HALO WV cross-section (Figure 6d) show a narrow filament of dry air ( $< 0.5 \text{ g/kg}$ )  
441 extending downward from 6 km at 01 UTC on 23 April to the top of the stratocu layer at approximately 01.5 UTC,  
442 which is correlated with the jet streak observed by DAWN.

443 A high pressure region with forecasted weak wind flow and low total precipitable water (Figure 5d) was  
444 sampled to the west along the triangular portion of the flight track, where a large region of low stratocu with varying  
445 thickness and morphology were present. The aerosol distribution was complex during this timeframe with high aerosol  
446 backscatter within the PBL overlaid by tenuous aerosol enhancements extending up to flight level (Figure 6c). These  
447 aerosol layers exhibit a high level of correlation between the wind speed, direction, and water vapor fields and provide  
448 insight into the complex interaction between atmospheric state, composition, and dynamics. A layer of relatively low  
449 aerosol backscatter with some vertical variability persisted from 2 to 4 km altitude which provided insufficient signal  
450 for DAWN wind retrieval. The flight progressed southeastward along the Aeolus track to a region of very dry air at  
451 the southern-most edge of the line. This dry air is depicted in the GOES WV imagery in Figure 1b and can also be  
452 seen in the HALO WV cross-section near 3 UTC, where mixing ratio below  $0.1 \text{ g/kg}$  at 4 km was observed. DAWN,  
453 and to a lesser extent MERRA, wind profiles agreed well with sondes, as shown by the four sonde comparisons in  
454 Figure 7.

455 After the Aeolus under flight near 02.5 UTC (white arrow, Figure 1b), the DC-8 proceeded northeast and  
456 again encountered the tropopause fold which exhibited similar vertical structure as the leg three hours prior during the  
457 outbound transit to the Aeolus underpass. The PBL depth and WVMR rose significantly after 04 UTC as the DC-8



458 transitioned from ocean back to land, spatial gradients of which were depicted by the 6-hour GEOS-5 forecast (Figure  
459 5c-d). Mountain waves of various orientations can be seen along the flight track in the contrast-enhanced GOES-17  
460 WV image (Figure 8a) after the flight traversed southeast of Santa Catalina Island. Complex wind, WV and aerosol  
461 distributions were present in association with the waves within the 0-4 km layer. A layer of high aerosol backscatter  
462 and weak ( $< 5$  m/s) winds was located in the lowest 0.75 km of the cross section from 04 to 04.6 (0400-0436) UTC  
463 as the flight approached the Peninsular Range along the California coast (Figures 8a-c). A shallow layer of  $\sim 12.5$  m/s  
464 westerly wind with reduced aerosol and drier air (Figure 8d) around 1 km altitude was beneath a filament of higher  
465 aerosol, weaker winds, and increased moisture that extended up to 2 km. Embedded wave structures can be seen in  
466 the aerosol backscatter from 04.4 to 04.6 UTC.

467 As the flight proceeded along the US-Mexico border and then turned northward, it transected near the center  
468 of the low pressure system (Figure 5a-b). This can be seen in the DAWN wind direction data before and after 05 UTC  
469 in Figure bb, where wind direction changes from northwesterly (magenta) to southeasterly (red to yellow), and wind  
470 speed reduced throughout the depth of the column. The GEOS-5 forecast indicated that the PBL height exceeded 3.5  
471 km across southern California and western Arizona (Figure 5c), which is consistent with HALO derived MLHs.  
472 WVMRs up to  $7$  g/kg and enhanced aerosol backscatter were observed upwards of 4 km altitude over the complex  
473 mountainous terrain due to orographic lifting. Deep convection had occurred earlier in the day in Arizona and had  
474 decayed by the time the DC-8 sampled the region, leaving the remnant anvil cloud observed in the HALO aerosol  
475 backscatter at 05.25 UTC. The low pressure system was associated with a depression of the tropopause, which reached  
476 a 10 km altitude. The stratospheric layer atop this low pressure system can be seen in the HALO WV data as extremely  
477 dry air ( $< 0.007$  g/kg) from  $\sim 04.5$  to 05.75 UTC, approximately 3 orders of magnitude drier than the PBL airmass below.  
478 This transect through the stratospheric intrusion was an ideal opportunity to showcase the capability of HALO in  
479 measuring over four orders of magnitude in WVMR from the moist PBL to the dry upper troposphere/lower  
480 stratosphere.

481 After sampling the stratospheric intrusion, the flight progressed northward into Utah before turning west  
482 across Nevada along the jet streak that was previously sampled across California. Mountain waves were also evident  
483 in GOES WV imagery across western Nevada near 06 UTC (Figure 1b), which can also be seen via wave structures  
484 in layers of enhanced aerosol and water vapor measured by HALO, and DAWN wind direction variations, that  
485 extended up to 9 km altitude. After 06.3 UTC on the western side of the Sierra Madre, the DC-8 flew through the



486 Central Valley region of California while descending to land in Palmdale, where there was a notable enhancement of  
487 aerosol backscatter in the PBL with weak wind flow, and complex vertical aerosol structures aloft.

488

#### 489 **4.3 25-28 April 2019**

490 The goals of the third and fourth flights of the Aeolus campaign focused on evaluating the performance of DAWN  
491 and HALO from the mid-latitudes to the tropics and also to the transition of wind, WV, aerosol, and cloud fields from  
492 the sub-tropics to deep tropics. The third flight on April 25-26 took a southwesterly heading to 7° N, 133° W, then  
493 descended as it progressed westward through the tropics at an 8 km altitude, before ascending and intersecting with  
494 the Aeolus track along a north-northwesterly heading before landing in Kona, Hawaii (Figure 1c). The sub-tropical  
495 jet stream can be observed in the DAWN wind speed as the DC-8 transitioned from the mid-latitude down to the east-  
496 west tropical line (Figure 9a). The tropical jet extends down to approximately 6 km which correlates extremely well  
497 with the top of elevated moist layer observed in the HALO WV profiles at approximately 22.5 UTC (Figure 9d). As  
498 the DC-8 proceeded westward towards the start of the Aeolus line, the mid-troposphere moist layer strengthened and  
499 deepened, and a weak overturning circulation associated with convective detrainment could be observed in the WV  
500 distributions, evidenced by the moist layer at and above ~8 km altitude extending northward from the deep tropics.  
501 HALO's ability to measure and infer dynamical processes via high vertical resolution WV and aerosol measurements  
502 is critical for improved understanding of the radiative transfer that drives large scale circulation, which can in turn  
503 effect low tropospheric stability, cloud formation, and convective aggregation (Stevens et al 2017, Holloway et al.  
504 2017, Mapes et al. 2017, Lebsack et al. 2017).

505 Another area of interest during this flight was the long north-south transect from Palmdale to the tropics  
506 where a variety of stratocu morphologies were present along flight track (Figure 10a), from closed cell to open cell  
507 stratocu in the northern part of the domain (20 to 20.8 UTC), then a combination of clear sky and small closed cell  
508 (20.8 to 21.6 UTC), and finally a larger closed cell with a different appearance than the previously observed clouds  
509 (21.6 to 22.5 UTC). Though wind speed was generally within the 0-10 m/s range within and above these clouds, the  
510 wind direction, aerosol, and water vapor profiles varied significantly as seen from the DAWN and HALO data in  
511 Figure 10. For example, a relatively moist airmass above the PBL and a shallow PBL depth was associated with the  
512 stratocu from 20-20.8 UTC (Figure 10e-f). Sharp directional wind shear in the 0 to 3 km layer was present around  
513 20.3 UTC during a brief transition to open cell stratocu (Figure 10c). Dry, high aerosol backscatter air with slightly



514 higher wind speed was found above the PBL from 20.8-21.6, leading to clear sky and broken clouds. The PBL depth  
515 and cloud top height grew with the differently textured closed cell clouds that were later encountered from 21.6 to  
516 22.5 UTC.

517 Prior to 22 UTC, some thin cirrus associated with the subtropical jet stream was encountered at flight level,  
518 which inhibited HALO profiling below 6 km. Cirrus were also encountered later in the flight around 23, 01, and 03-  
519 05 UTC. Additionally, ice accretion on the HALO window resulted in significant near field signal and contaminated  
520 the 532 nm cross-polarization channel. Similar near field signals were also observed on the subsequent return flight  
521 from Kona back to Palmdale. As a result, the HSRL measurement for both of the tropical flights are limited to only  
522 use the co-polarization channels resulting in limited retrievals of aerosol intensive parameters such as depolarization,  
523 spectral depolarization ratio, and aerosol type. In order to increase sensitivity and enable wind retrieval in low aerosol  
524 conditions encountered after 21.25 UTC correlated with increasing moisture aloft within a sub-tropical airmass,  
525 DAWN was operated in a 2-azimuth, 200 pulse/azimuth mode from 22.4 to 23.6 UTC. This change helped to provide  
526 greater vertical coverage of winds at middle levels of the cross section, though Figure 10d shows that vertical  
527 integration at a variety of depths was still required to achieve sufficient signal for wind retrieval. A sonde was released  
528 at 22.6 UTC where HALO observed weak aerosol signal in the 1.5 to 6 km layer. Despite this weak signal and vertical  
529 integration required to achieve enough signal for wind retrieval, DAWN retrieved a full wind profile that agreed quite  
530 well with the sonde (Figure 11).

531 As noted above, after 23 UTC, deep tropical moisture was observed by HALO, with mixing ratios exceeding  
532 20 g/kg near the surface and exceeding 6 g/kg up to 6 km. The enhanced moisture content in the middle troposphere  
533 could be seen in GOES WV imagery via colder temperature, indicating WV absorption from higher altitudes (Figure  
534 1c). The tropical airmass featured weak aerosol scattering above 2 km which generally inhibited wind profiling within  
535 the 2-6 km layer. After 02 UTC, the plane ascended as it moved northwestward to head toward the Aeolus track.  
536 GOES WV imagery showed a sharp transition from moist to dry conditions as the aircraft crossed 10° N. This drying  
537 can be seen in the HALO data, where mixing ratio decreased from above 5 g/kg to below 1 g/kg above 4 km. An  
538 aerosol layer was present at 6 km which enabled wind retrieval for comparison with the Aeolus overpass in the 04-05  
539 UTC timeframe.

540 The 27-28 April flight from Kona featured similar conditions to the 25-26 April flight, with tropical moisture  
541 within and above the PBL in a relatively clean atmosphere void of significant aerosol enhancements. This flight was



542 designed to transect through the northern half of the ITCZ in an attempt to sample the ascending branch of the Hadley  
543 circulation (Figure 1d). Furthermore, several diagonally-oriented transects allowed for testing and optimization of the  
544 HALO DIAL measurements over a wide range of mid-lower tropospheric WV concentrations, demonstrating the  
545 ability of the WV DIAL to optimize the WV absorption as a function of latitude and moisture content. Although  
546 HALO was able to demonstrate the required spectral tuning to maintain good measurement precision over the mid-  
547 latitude and subtropical environments, the required amount of spectral tuning required for precise measurements in  
548 the tropics was not achieved. This was overcome by increasing the vertical averaging within the lower free troposphere  
549 and PBL from 315 m to 585 m. The additional spectral tuning required to achieve high precision and vertical  
550 resolution in the tropics is currently under investigation and will be implemented for future campaigns.

551 The DAWN and HALO wind, WV and aerosol backscatter cross-sections are shown in Figure 12. The  
552 subtropical jet was observed by DAWN with upper level winds exceeding 30 m/s above 10 km (Figure 12a). DAWN  
553 data show good vertical coverage despite the low aerosol loading throughout the middle free troposphere (Figure 12c).  
554 As with the previous flight, the HALO WV and aerosol fields show a high level of correlation where the vertical  
555 gradients of WV enhancements throughout the mid-troposphere were often correlated with gradients in aerosol  
556 backscatter (Figure 12c-d). These gradients are likely associated with advected air masses and show the utility of  
557 using WV and aerosol fields as atmospheric tracers for large scale motion. As with the 25-26 April flight, moistening  
558 of the mid-troposphere was observed as the DC-8 approached the ITCZ. The HALO WV cross-sections near the  
559 tropics around 20 UTC (~6 N) again show evidence of overturning circulation to the higher latitudes resulting from  
560 convective mid-level detrainment near the ITCZ.

561

#### 562 **4.4 29-30 April 2019**

563 The final flight of the campaign sampled a similar geographic region to the oceanic portion of the 22-23 April flight,  
564 and was focused on analyzing atmospheric spatial and temporal variability, instrument performance, and dropsonde  
565 and HALO WV profile validation (Figure 1e). The flight began with a segment beneath 5 km extending into  
566 southeastern California, near to regions of developing convection within an upper-level low. HALO WV mixing ratio  
567 in this region reached 8 g/kg which provided sufficient moisture for development of deep convection (Figure 13d).  
568 The aircraft ascended to above 9 km and crossed through the western edge of the cyclonic circulation, where a deep  
569 layer of northerly winds exceeding 20 m/s were present (Figure 13a).



570 The flight progressed to a region with optically thick and spatially uniform stratocu where the aircraft  
571 decreased altitude to near 3 km above sea level. The aircraft carried out a stair-step flight pattern at five different  
572 altitudes over this same region (region bracketed by circles in the center of GOES imagery in Figure 1e), ascending  
573 by approximately 1.8 km in flight level with each pass. The intent of this flight pattern was to look at the repeatability  
574 of the lidar measurements over the same airmass and also assess the DAWN sensitivity to aerosol backscatter with  
575 increasing flight altitude. The HALO WV and aerosol observations show very persistent, repeating patterns as the  
576 aircraft transected the same region at different altitudes (Figure 13c-d). Extremely dry air was present just above the  
577 stratocu tops near 2 km within a strong capping inversion (not shown), a feature which was pervasive throughout the  
578 flight and could have been caused by a combination of radiative cooling near cloud top and subsidence, similar to the  
579 18 April flight. The symmetry isn't quite as prominent in the DAWN data due to frequent turns, but it can be seen that  
580 winds were continually retrieved from aircraft to stratocu cloud top until the aircraft reached 10.5 km altitude.

581 The flight left this stratocu region around 23.75 UTC and progressed westward to another area with clear sky  
582 to broken clouds at 0.25 UTC (24.25 UTC on the lidar time series) to carry out lidar overpasses near an in situ spiral  
583 location to validate the HALO WV measurements against the DLH open path measurements. As the DC-8 approached  
584 the sampling area it was vectored by air traffic control which resulted in altitude changes around 0.3 and 0.8 UTC.  
585 The aircraft descended down to 8 km, flew over this region, then ascended to 10 km and again flew over the same  
586 region. A sonde was released during both transects, one corresponding to the center of the north-south leg and the  
587 other closer to the location of a spiral near the north end of the leg. Upon a final pass near the sampling region on the  
588 north end of the leg, the aircraft spiraled from flight altitude at ~10 km down to ~150 m above the ocean surface.  
589 During this time the NASA LaRC DLH instrument was collecting in situ WV observations which were used to assess  
590 the performance of the HALO and sonde derived WV profiles within the same region.

591 Examples of these comparison profiles between the three measurements during the descending leg of the  
592 spiral are shown in Figure 14. Figure 14a shows the comparison between the sonde and the DLH profile. As  
593 previously discussed, the slow response time of the humidity sensor after deployment from the DC-8 limited  
594 meaningful observations until ~5 km above the surface. The damped response time is also evident throughout the  
595 lower troposphere resulting in disagreement in prominent features compared to DLH. It should, however, be noted  
596 that the moisture field within the comparison region was quite variable and some of the disagreement could result  
597 from mismatch in sampling volumes between the two measurements. It should also be noted that only the edge of the



598 in-situ spiral overlapped with the multiple DC-8 remote sensing tracks and that the location of the spiral was also  
599 offset to the northern end of the track. Furthermore, the diameter of the in situ spiral was approximately  $\frac{1}{4}$  the width  
600 of the entire comparison track and substantial variability was observed within this volume which could explain the  
601 high frequency variability in the DLH data around 4 km.

602           Figures 14b-c show the comparison between the HALO and DLH WV measurements at two different  
603 locations along the remote sensing tracks. These comparisons were carried out at the higher 315 m vertical resolution  
604 as there was sufficient aerosol loading throughout the troposphere allowing for higher resolution retrievals. For each  
605 comparison, two independently retrieved profiles were joined using a 315 m weighted average. This was carried out  
606 to overcome the mismatch in the sampling volumes as well as the variability in the WV field along the aircraft track  
607 and provide a fair comparison between the two measurements. The top portion of the profile for the comparisons in  
608 Figure 14b-c are from 0123 UTC and extends to the highest altitude right before the start of the spiral. In both  
609 comparisons the top profile is used until the bottom profile is available, at which point the 315 m weighted average is  
610 carried out. The weighted average is applied from 8154 to 7839 m and 7090 to 6775 m for the comparisons in Figure  
611 14b, and c, respectively. The comparison between HALO and DLH in both instances show very good agreement and  
612 provide confidence in the validity of the measurements throughout the duration of the Aeolus campaign. Sonde  
613 calibration efforts are ongoing and a HALO WV validation paper is currently in development and will provide further  
614 details on HALO performance.

615           After completing the descending in situ profile, the aircraft spiraled upward to 10 km and reached the Aeolus  
616 overpass at 02.2 UTC where it stayed along the overpass track until near 03 UTC. Very intricate structures in the  
617 WV, aerosol, and wind fields were observed along the entire Aeolus underpass. Winds gradually accelerated to near  
618 30 m/s along the overpass where a narrow jet streak with very low aerosol backscatter conditions was sampled near 3  
619 UTC. This jet streak also resulted in transport of moisture from the mid-lower troposphere to the aircraft altitude (see  
620 layer between 03-04 UTC above 8 km). The DC-8 then proceeded directly back to Palmdale to complete the flight  
621 campaign.

622

#### 623 **4.6 DAWN Validation**

624           Figures 4, 7, and 11 show that DAWN winds agreed quite well with sonde regardless of wind speed, though  
625 some differences are evident. Differences should not necessarily be interpreted as “errors” because DAWN and sonde



626 measure winds at differing time and spatial scales, in addition to the fact that sondes drift away from the aircraft flight  
627 track into regions not sampled by DAWN. Histograms of DAWN-sonde wind speed and direction differences are  
628 shown in Figures 15a-b based on comparison of 61 time-matched sondes, encompassing up to 12,260 DAWN vertical  
629 levels. Both the wind speed and directional accuracy (e.g. bias) were minimal at 0.12 m/s and 1.02°, respectively.  
630 Precision (i.e. root-mean-squared difference or RMSD) was 1.22 m/s and 7.6° for speed and direction, respectively.  
631 Wind direction precision decreased with decreasing wind speed, and differences reached up to 30° for wind speed less  
632 than 5 m/s (Figure 15c). This is to be expected to some extent given that weak wind flows can have variable wind  
633 direction over the typical observation/comparison periods discussed here. Wind component differences from the sonde  
634 ranged from 1.17 (v-component, red line) to 1.29 m/s (u-component, blue line), which differed from the 2017 CPEX  
635 campaign (Greco et al. 2020) where ~1.6 m/s RMSD for both components were found. However, sondes were released  
636 within and near convection during CPEX 2017 where increased spatial wind variability occurs, relative to the more  
637 quiescent conditions during the Aeolus Cal/Val campaign. These results further reinforce the conclusion of Greco et  
638 al. (2020), in that coherent airborne doppler wind lidar can deliver to the atmospheric research and operational  
639 forecasting communities a low bias wind profile from 10+ km altitude with a high vertical resolution every 2-10 km  
640 along the ground track (aircraft airspeed dependent), aerosols and clouds permitting. The combination of high  
641 resolution, accuracy, and precision of the DAWN and HALO data, make these data extremely useful for atmospheric  
642 and cloud process studies, and Aeolus validation.

643

#### 644 **4.7 DAWN Comparisons with Aeolus**

645 Aeolus Level 2B Rayleigh clear HLOS and DAWN HLOS cross sections and profile comparisons with sonde at the  
646 time of the Aeolus overpass from the 30 April flight are shown in Figures 16a-b. Due in part to the issues described  
647 in Section 2, as well as the fact that Aeolus is measuring winds from a 320 km orbit distance, the Aeolus cross section  
648 shows much greater random variability than the DAWN cross section. This is further depicted in the profile  
649 comparison (Figure 16c), where a 90 km mean DAWN profile and sonde wind speed profile (projected to the Aeolus  
650 LOS), agree extremely well but Aeolus often falls outside of the variance in each Aeolus vertical layer measured by  
651 DAWN. Rayleigh clear HLOS and DAWN HLOS cross sections for the other four flights are shown in Figure 17,  
652 which again illustrate random variability in the Aeolus data relative to the more smooth and spatially-coherent DAWN  
653 winds. A scatter diagram of Aeolus Level 2B and DAWN HLOS comparisons is shown in Figure 18, encompassing



654 231 vertical levels of Aeolus Rayleigh clear and 42 levels of Mie cloudy vertical bins using methods described in  
655 Section 2.4. Aeolus Rayleigh clear had a high wind speed bias of 1.19 m/s and a RMSD of 5.14 m/s. Aeolus Mie  
656 cloudy had a high bias of 1.98 m/s and RMSD of 4.68 m/s. As mentioned in Section 2.4, it should be noted here that  
657 the validated Aeolus L2B dataset is known to contain wind speed biases caused by an imperfect telescope temperature  
658 management along the orbit and from orbit to orbit, pending the top of the atmosphere total radiance variability. This  
659 has been shown from ECMWF model observation monitoring and from comparisons with ground-based and  
660 radiosonde observations (Martin et al 2020). These results differ from those reported by Witschas et al. (2020) during  
661 WindVal III and AVATARE, which could be caused by a variety of factors including differences in Aeolus laser pulse  
662 energy and latitude, longitude, and time-dependent telescope temperature issues at the time of the campaigns, wind  
663 conditions being sampled, sample size, and criteria used to construct the Aeolus – airborne wind lidar match database.  
664 As mentioned previously, since the time that this Aeolus data was produced, numerous corrections to address various  
665 instrument and data issues have been developed. Extensive validation of Aeolus is not possible here due to the  
666 relatively small sample size of co-located data and preliminary nature of the Aeolus products. We expect that future  
667 reprocessing of Aeolus data with improved bias correction and also greater output power from Aeolus Laser-B will  
668 result in better data quality with improved agreement with air- and ground-based wind observations.

669

## 670 **5. Summary and Future Work**

671 This paper summarized DAWN and HALO lidar observations and the wide variety of atmospheric phenomena  
672 sampled during the April 2019 Aeolus Cal/Val Test Flight campaign across the eastern Pacific Ocean. Though this  
673 campaign focused on regional surveys to characterize instrument performance rather than detailed process studies,  
674 phenomena and conditions sampled during the campaign were relatively unique for DAWN, in addition to this being  
675 the first flight where HALO operated in WV profiling mode. It was found that DAWN and HALO resolved complex  
676 and detailed vertical structures and horizontal gradients associated with a variety of phenomena including mid-latitude  
677 cyclones, jet streaks and tropopause folds, mountain waves, large scale tropical circulation, and variability associated  
678 with changing stratocumulus cloud patterns. More focused case studies analyzing some of these features are planned  
679 for future publication. DAWN wind retrievals generally coincided with areas of enhanced HALO aerosol backscatter  
680 and demonstrated excellent agreement with sonde throughout the campaign. Though we were not able to validate  
681 HALO WV profiles with sonde profiles due to sonde performance issues, validation using DLH in-situ WV data



682 during a spiral down to near the ocean surface indicated excellent agreement. Comparison with DLH indicated that  
683 extremely low WVMR above stratocumulus cloud top observed by HALO during two flights was a real phenomenon,  
684 highlighting how WV DIAL and HSRL can be used in future PBL and cloud-focused studies to resolve fine scale  
685 features that are challenging for other passive retrieval methods. Aeolus, which had been encountering performance  
686 issues and other technical challenges from the time of launch through when our campaign was conducted, provided  
687 winds that differed from DAWN more than in other recent European Aeolus Cal/Val campaigns involving the DLR  
688 2-micron coherent wind lidar. We anticipate improved agreement with DAWN when Aeolus Level 2B data is  
689 reprocessed in the future.

690 This campaign provided an initial demonstration of how cloud and weather phenomena coincide with and  
691 are modulated by variations in wind, WV, and aerosol conditions, and how such variations can be observed by airborne  
692 lidar instruments. High precision and detailed measurements of these variables, in addition to many others such as  
693 temperature, cloud microphysics, and precipitation profiles, are required to address key science questions posed by  
694 the 2017 Earth Science Decadal Survey (ESAS 2017). Airborne sensors and campaigns like this Aeolus Cal/Val Test  
695 Flight campaign are needed to collect data of sufficient precision and detail to supplement and evaluate the  
696 performance of existing space-borne sensors.

697 The upcoming Convective Processes Experiment – Aerosols and Winds (CPEX-AW) campaign, scheduled  
698 to occur in July-August 2021 and intended to operate out of Sal Island of Cabo Verde, will build upon understanding  
699 of convective processes that has been gained from 2017 CPEX campaign datasets and models. DAWN, HALO,  
700 dropsondes, the Airborne Precipitation and cloud Radar – 3<sup>rd</sup> Generation (APR-3), and the High Altitude Monolithic  
701 Microwave integrated Circuit Sounding Radiometer (HAMSR, Brown et al. 2011) instruments will fly aboard the DC-  
702 8 during CPEX-AW. CPEX-AW, in conjunction with the international Aeolus Tropical Campaign, will conduct flight  
703 segments focused on Aeolus Cal/Val in addition to other segments to address a number of science goals including: 1)  
704 investigating how convective systems interact with lower tropospheric and surface winds in the intertropical  
705 convergence zone (ITCZ), 2) determining the role of aerosols, WV, winds, clouds, and precipitation and their  
706 interactions with African weather and air quality, 3) measuring the vertical structures and variability of WV, winds,  
707 and aerosols within the boundary layer and their coupling to convection initiation and lifecycle in the ITCZ, 4)  
708 studying how the African easterly waves and Sahara Air Layer (dry air and dust) control the convectively suppressed  
709 and active periods of the ITCZ. In preparation for CPEX-AW, we are continuing to improve DAWN through better



710 detector response, faster scanning between azimuths, and adjustment to DAWN scanning patterns which will result in  
711 improved aerosol sensitivity, and higher spatial sampling of wind profiles and improved resolution of mesoscale wind  
712 flows. HALO improvements for CPEX-AW include optimization of detector gain settings for improved SNR and  
713 increasing the offset locking bandwidth of the PBL weighted transmitted wavelength to allow for optimization of the  
714 water vapor optical depth and hence, precision within the tropical and subtropical latitudes.

715

## 716 **6. Acknowledgements**

717 We acknowledge directed funding support from the NASA Headquarters Earth Science Division that covered  
718 execution of the flight campaign and subsequent data analysis. We thank the DC-8 team at the NASA Armstrong  
719 Flight Research Center and the National Suborbital Education and Research Center at the University of North Dakota  
720 for their excellent execution of the campaign. We thank the following people from NASA Langley Research Center,  
721 Anthony Notari and David Harper for the heroic effort integrating and testing HALO prior to the campaign, Joseph  
722 Lee for his time and effort integrating and operating HALO during the campaign, Larry Petway, John Marketon, Dave  
723 Macdonnell, Charles Trepte, Sam Chen, Jay Yu, Abou Traore, Connor Huffine, Seth Begay, Anna Noe, Diego  
724 Pierrottet, Alan Little, and Eric Altman for their incredible efforts in preparing and testing DAWN prior to deployment,  
725 improving instrument performance, integrating onto the DC-8, operating throughout the campaign, and supporting  
726 science investigations, Glenn Diskin and Joshua Digangi for providing DLH data used to validate HALO WV  
727 observations, and Christopher Yost, Douglas Spangenberg, Thad Chee, and Louis Nguyen for providing forecasting  
728 and flight planning support for the campaign. We also thank Sammy Henderson of Beyond Photonics for his expertise  
729 with characterizing DAWN performance prior to integration. We thank Anne Grete Straume-Linder and Sebastian  
730 Bley (ESA), and Oliver Reitebuch (DLR) for their contributions to description of the Aeolus mission and ALADIN  
731 status. We thank Will McCarty and the NASA GMAO for providing GEOS-5 forecast products over the flight  
732 campaign domain. We thank the Data Center at the University of Wisconsin-Madison Space Science Engineering  
733 Center for providing GOES-17 imagery and NOAA NESDIS for granting 1-minute GOES-17 Mesoscale Domain  
734 Sectors throughout the campaign. DAWN, HALO, and dropsonde datasets described in this paper can be accessed at  
735 the NASA Langley Atmospheric Science Data Center: <https://asdc.larc.nasa.gov/project/Aeolus>

736

737



738 **7. References**

739 Asrar, G., and Coauthors, 2015: Climate Symposium 2014: Findings and Recommendations. *Bull. Amer. Meteor.*  
740 *Soc.*, 96, ES145–ES147, <https://doi.org/10.1175/BAMS-D-15-00003.1>.

741

742 Baars, H., Herzog, A., Heese, B., Ohneiser, K., Hanbuch, K., Hofer, J., Yin, Z., Engelmann, R., and Wandinger, U.,  
743 2020: Validation of Aeolus wind products above the Atlantic Ocean, *Atmos. Meas. Tech. Discuss.*,  
744 <https://doi.org/10.5194/amt-2020-198>, in review.

745

746 Black, P., L. Harrison, M. Beaubien, R. Bluth, R. Woods, A. Penny, R.W. Smith, and J.D. Doyle, 2017: [High-](#)  
747 [Definition Sounding System \(HDSS\) for Atmospheric Profiling](#). *J. Atmos. Oceanic Technol.*, 34, 777–  
748 796, <https://doi.org/10.1175/JTECH-D-14-00210.1>

749

750 Braun, S. A., and Coauthors, 2013: NASA's Genesis and Rapid Intensification Processes (GRIP) Field  
751 Experiment. *Bull. Amer. Meteor. Soc.*, **94**, 345–363, <https://doi.org/10.1175/BAMS-D-11-00232.1>.

752

753 Browell, E., and Co-authors, 1997: LASE validation experiment, in *Advances in Atmospheric Remote Sensing with*  
754 *Lidar*, A. Ansmann, R. Neuber, P. Rairoux, and U. Wandinger, eds., Springer-Verlag, Berlin, 289-295.

755

756 Brown, S. T.; Lambigtsen, B.; Denning, R. F.; Gaier, T.; Kangaslahti, P.; Lim, B. H.; Tanabe, J. M.; Tanner, A. B.,  
757 2011: The High-Altitude MMIC Sounding Radiometer for the Global Hawk Unmanned Aerial Vehicle: Instrument  
758 Description and Performance. *IEEE Transactions on Geoscience and Remote Sensing*; doi:  
759 10.1109/TGRS.2011.2125973

760

761 Bucci, L.R.; O'Handley, C.; Emmitt, G.D.; Zhang, J.A.; Ryan, K.; Atlas, R., 2018: Validation of an Airborne Doppler  
762 Wind Lidar in Tropical Cyclones. *Sensors*, *18*, 4288.

763



764 Burton, S. P., Ferrare, R. A., Hostetler, C. A., Hair, J. W., Rogers, R. R., Obland, M. D., Butler, C. F., Cook, A. L.,  
765 Harper, D. B., and Froyd, K. D., 2012: Aerosol classification using airborne High Spectral Resolution Lidar  
766 measurements – methodology and examples, *Atmos. Meas. Tech.*, 5, 73–98, doi:10.5194/amt-5-73-2012  
767

768 Cui, Z., Z. Pu, G. D. Emmitt, and S. Greco, 2020: The Impact of Airborne Doppler Aerosol Wind (DAWN) Lidar  
769 Wind Profiles on Numerical Simulations of Tropical Convective Systems during the NASA Convective Processes  
770 Experiment (CPEX). *J. Atmos. Oceanic Technol.*, 37, 705–722, <https://doi.org/10.1175/JTECH-D-19-0123.1>.  
771

772 Diskin, G. S., J. R. Podolske, G. W. Sachse, T. A. Slate, 2002: Open-path airborne tunable diode laser hygrometer,  
773 *Proc. SPIE 4817, Diode Lasers and Applications in Atmospheric Sensing*; <https://doi.org/10.1117/12.453736>  
774

775 Doyle, J. D., and Co-authors, 2017: A View of Tropical Cyclones from Above: The Tropical Cyclone Intensity  
776 Experiment. *Bull. Amer. Meteor. Soc.*, 98, 2113–2134, <https://doi.org/10.1175/BAMS-D-16-0055.1>.  
777

778 DuVivier, A. K., J. J. Cassano, S. Greco, and G. D. Emmitt, 2017: A Case Study of Observed and Modeled Barrier  
779 Flow in the Denmark Strait in May 2015. *Mon. Wea. Rev.*, 145, 2385–2404, <https://doi.org/10.1175/MWR-D-16-0386.1>.  
780

781

782 ESA, 2016: ADM-Aeolus Mission Requirements Document.  
783 Available online at: [https://esamultimedia.esa.int/docs/EarthObservation/ADM-Aeolus\\_MRD.pdf](https://esamultimedia.esa.int/docs/EarthObservation/ADM-Aeolus_MRD.pdf)  
784

785 ESA, 2019: Aeolus Scientific Calibration and Validation Implementation Plan. Available online at:  
786 <https://earth.esa.int/pi/esa?id=4910&sideExpandedNavigationBoxId=Aos&cmd=image&topSelectedNavigationNodeId=AOS&targetIFramePage=/web/guest/pi-community/apply-for-data/aos&ts=1606751895912&type=file&colorTheme=03&sideNavigationType=AO&table=aotarget>  
787  
788  
789

790 ESAS, 2017: [https://www.nationalacademies.org/our-work/decadal-survey-for-earth-science-and-applications-from-](https://www.nationalacademies.org/our-work/decadal-survey-for-earth-science-and-applications-from-space)  
791 [space](https://www.nationalacademies.org/our-work/decadal-survey-for-earth-science-and-applications-from-space)



792

793 Flamant, P., Cuesta, J., Denneulin, M. L., Dabas, A., Huber, D., 2008: ADM-Aeolus retrieval algorithms for aerosol  
794 and cloud products. *Tellus A*, 60, 273–288.

795

796 Gelaro, R., W. McCarty, M. Suarez, R. Todling, A. Molod, L. Takacs, C. Randles, A. Darmenov., M. Bosilovich, R.  
797 Reichle, 2017: The Modern-Era Retrospective Analysis for Research and Applications, Version 2 (MERRA-2), J.  
798 Clim., 30, 5419-5454 [doi: 10.1175/JCLI-D-16-0758.1](https://doi.org/10.1175/JCLI-D-16-0758.1)

799

800 Greco, S.; Emmitt, G.D.; Garstang, M.; Kavaya, M. Doppler Aerosol WiNd (DAWN) Lidar during CPEX 2017, 2020:  
801 Instrument Performance and Data Utility. *Remote Sens.* **2020**, *12*, 2951.

802

803 Hair, J. W., C. A. Hostetler, A. L. Cook, D. B. Harper, R. A. Ferrare, T. L. Mack, W. Welch, L. R. Izquierdo, and F.  
804 E. Hovis, 2008: Airborne High Spectral Resolution Lidar for profiling aerosol optical properties, *Appl. Opt.* 47, 6734-  
805 6752

806

807 Henderson, S. W., P.Gatt, D. Rees, and R. M. Huffaker, 2005: Wind lidar. *Laser Remote Sensing*, T. Fujii and T.  
808 Fukuchi, Eds., CRC Taylor and Francis, 469–722.

809

810 Holloway, C.E., Wing, A.A., Bony, S., and Co-authors, 2017: Observing Convective Aggregation. *Surv*  
811 *Geophys* 38, 1199–1236 (2017). <https://doi.org/10.1007/s10712-017-9419-1>

812

813 Ismail, S., and E. V. Browell, 1989: Airborne and spaceborne lidar measurements of water vapor profiles: a sensitivity  
814 analysis, *Appl. Opt.* 28, 3603-3615.

815

816 Kanitz, T., Lochard, J., Marshall, J., McGoldrick, P., Lecrenier, O., Bravetti, P., Reitebuch, O., Rennie, M., Wernham,  
817 D., and Elfving, A., 2019: Aeolus first light: first glimpse, in: Proc. SPIE 11180, International Conference on Space  
818 Optics – ICSO 2018, 111801R, <https://doi.org/10.1117/12.2535982>

819



- 820 Kavaya, M. J., J. Y. Beyon, G. J. Koch, M. Petros, P. J. Petzar, U. N. Singh, B. C. Trieu, and J. Yu, 2014: The Doppler  
821 Aerosol Wind (DAWN) Airborne, Wind-Profiling Coherent-Detection Lidar System: Overview and Preliminary  
822 Flight Results. *J. Atmos. Oceanic Technol.*, **31**, 826–842, <https://doi.org/10.1175/JTECH-D-12-00274.1>.  
823
- 824 Khaykin, S. M., Hauchecorne, A., Wing, R., Keckhut, P., Godin-Beekmann, S., Porteneuve, J., Mariscal, J.-F., and  
825 Schmitt, J.: Doppler lidar at Observatoire de Haute-Provence for wind profiling up to 75 km altitude: performance  
826 evaluation and observations, *Atmos. Meas. Tech.*, **13**, 1501–1516, <https://doi.org/10.5194/amt-13-1501-2020>, 2020.  
827
- 828 Koch, G. J., J. Y. Beyon, E. A. Modlin, P. J. Petzar, S. Woll, M. Petros, J. Yu, and M. J. Kavaya, 2012: Side-scan  
829 Doppler lidar for offshore wind energy applications. *J. Appl. Remote Sens.*, **6**, 063562, doi:10.1117/1.JRS.6.063562.  
830
- 831 Lebsock, M.D., L'Ecuyer, T.S. & Pincus, R., 2017: An Observational View of Relationships Between Moisture  
832 Aggregation, Cloud, and Radiative Heating Profiles. *Surv Geophys* **38**, 1237–1254 (2017).  
833 <https://doi.org/10.1007/s10712-017-9443-1>  
834
- 835 Lux, O., Lemmerz, C., Weiler, F., Marksteiner, U., Witschas, B., Rahm, S., Schäfler, A., and Reitebuch, O., 2018:  
836 Airborne wind lidar observations over the North Atlantic in 2016 for the pre-launch validation of the satellite mission  
837 Aeolus, *Atmos. Meas. Tech.*, **11**, 3297–3322, <https://doi.org/10.5194/amt-11-3297-2018>  
838
- 839 Lux, O., Lemmerz, C., Weiler, F., Marksteiner, U., Witschas, B., Rahm, S., Geiß, A., and Reitebuch, O., 2020:  
840 Intercomparison of wind observations from the European Space Agency's Aeolus satellite mission and the ALADIN  
841 Airborne Demonstrator, *Atmos. Meas. Tech.*, **13**, 2075–2097, <https://doi.org/10.5194/amt-13-2075-2020>  
842
- 843 Marksteiner, U., Ch. Lemmerz, O. Lux, S. Rahm, A. Schäfler, B. Witschas, O. Reitebuch (2018): Calibrations and  
844 Wind Observations of an Airborne Direct-Detection Wind LiDAR Supporting ESA's Aeolus Mission. *Remote*  
845 *Sensing*, **10**, 2056; <https://doi.org/10.3390/rs10122056>  
846



847 Martin, A., Weissmann, M., Reitebuch, O., Rennie, M., Geiß, A., and Cress, A.: Validation of Aeolus winds using  
848 radiosonde observations and NWP model equivalents, *Atmos. Meas. Tech. Discuss.*, <https://doi.org/10.5194/amt->  
849 2020-404, in review, 2020.

850

851 Mapes B., Chandra A.S., Kuang Z., Zuidema P., 2017: Importance Profiles for Water Vapor. In: Pincus R., Winker  
852 D., Bony S., Stevens B. (eds) *Shallow Clouds, Water Vapor, Circulation, and Climate Sensitivity*. Space Sciences  
853 Series of ISSI, vol 65. Springer, Cham

854

855 Measures, R. M., 1984: *Laser Remote Sensing: Fundamentals and Applications*, John Wiley, New York (1984),  
856 510 pages, ISBN 0471081930, 9780471081937.

857

858 NASA, 2017: <https://cpex.jpl.nasa.gov/about.php>

859

860 Nehrir A.R., Kiemle, C., Lebsock, M. D., and Co-authors, 2017: Emerging Technologies and Synergies for Airborne  
861 and Space-Based Measurements of Water Vapor Profiles. *Surv Geophys* 38, 1445–1482.  
862 <https://doi.org/10.1007/s10712-017-9448-9>

863

864 ----, Notari A., Harper D., Fitzpatrick F., Collins J., Kooi S., Antill C., Hare R., Barton-Grimley R., Hair J., Ferrare  
865 R., Hostetler C., Welch W., 2018: The High Altitude Lidar Observatory (HALO): A multi-function lidar and  
866 technology test-bed for airborne and space-based measurements of water vapor and methane. *Earth Science*  
867 *Technology Forum*, Silver Spring, MD.  
868 [http://www.estotechnology.us/techportfolio/pdf/additionalInfo/1914\\_Nehrir/Nehrir\\_ESTF2018\\_A1P2.pdf](http://www.estotechnology.us/techportfolio/pdf/additionalInfo/1914_Nehrir/Nehrir_ESTF2018_A1P2.pdf)

869

870 ----, Hair J. W., Ferrare R. A., Hostetler C. A., Kooi S. A., Notari A., Harper D. A., Collins, J. E., Jr., Barton-Grimley,  
871 R. A., Antill, C., Hare, R. J., and Fitzpatrick, F., 2018. The high altitude lidar observatory (HALO): a multi-function  
872 lidar and technology testbed for airborne and space-based measurements of water vapor and methane. *American*  
873 *Geophysical Union*, Fall Meeting 2018, abstract #A31P-3155.

874



875 ----, Hair, H., Ferrare R., Hostetler, C., Notari, A., Harper, D., Collins, J., Kooi, S., Barton-Grimley, R., Fitzpatrick,  
876 F., 2019: Airborne Lidar Observations of Water Vapor, Methane, and Aerosol/Cloud Profiles with the High Altitude  
877 Lidar Observatory. *AGU Fall Meeting, A43D-04*  
878

879 Reitebuch O., 2012: Wind Lidar for Atmospheric Research. In: Schumann U. (eds) *Atmospheric Physics. Research*  
880 *Topics in Aerospace*. Springer, Berlin, Heidelberg. [https://doi.org/10.1007/978-3-642-30183-4\\_30](https://doi.org/10.1007/978-3-642-30183-4_30)  
881

882 Reitebuch, O., Lemmerz, C., Lux, O., Marksteiner, U., Rahm, S., Weiler, F., Witschas, B., Meringer, M., Schmidt,  
883 K., Huber, D., Nikolaus, I., Geiß, A., Vaughan, M., Dabas, A., Flament, T., Stieglitz, H., Isaksen, L., Rennie, M., de  
884 Kloe, J., Marseille, G.-J., Stoffelen, A., Wernham, D., Kanitz, T., Straume, A.-G., Fehr, T., von Bismark, J.,  
885 Floberghagen, R., and Parrinello, T., 2019: Initial assessment of the performance of the first Wind Lidar in space on  
886 Aeolus. *EPJ Web Conf.*, 237 (2020) 01010. <https://doi.org/10.1051/epjconf/202023701010>  
887

888 Rennie, M. P., 2018: An assessment of the expected quality of Aeolus Level-2B wind products, *EPJ Web Conf.*, 176,  
889 02015, <https://doi.org/10.1051/epjconf/201817602015>  
890

891 Rennie, M. P. and Isaksen, L. 2020: The NWP impact of Aeolus Level-2B Winds at ECMWF. *ECMWF Technical*  
892 *Memorandum* 864. DOI: [10.21957/alift7mhr](https://doi.org/10.21957/alift7mhr). Available online at: <https://stage.ecmwf.int/node/19538>  
893  
894  
895

896 Scarino, A. J., Obland, M. D., Fast, J. D., Burton, S. P., Ferrare, R. A., Hostetler, C. A., Berg, L. K., Lefer, B., Haman,  
897 C., Hair, J. W., Rogers, R. R., Butler, C., Cook, A. L., and Harper, D. B., 2014: Comparison of mixed layer heights  
898 from airborne high spectral resolution lidar, ground-based measurements, and the WRFChem model during CalNex  
899 and CARES, *Atmos. Chem. Phys.*, 14, 5547–5560, doi:10.5194/acp-14-5547-2014  
900



- 901 Shipley S. T., D. H. Tracy, E. W. Eloranta, J. T. Tauger, J. T. Sroga, F. L. Roesler, and J. A. Weinman, 1983: High  
902 spectral resolution lidar to measure optical scattering properties of atmospheric aerosols. 1: Theory and  
903 instrumentation, *Appl. Opt.* 22, 3716–3724.  
904
- 905 Stevens, B., Brogniez, H., Kiemle, C., and Co-Authors, 2017: Structure and Dynamical Influence of Water Vapor in  
906 the Lower Tropical Troposphere. *Surv Geophys* 38, 1371–1397. <https://doi.org/10.1007/s10712-017-9420-8>  
907
- 908 Stith, J. L., and Co-authors, 2018: 100 Years of Progress in Atmospheric Observing Systems. *Meteor. Monogr.*, 59  
909 2.1–2.55. doi: <https://doi.org/10.1175/AMSMONOGRAPHS-D-18-0006.1>.  
910
- 911 Stoffelen, A., Pailleux, J., Kall'ën, E., Vaughan, J. M., Isaksen, I., Flamant, P., Wergen, W., Andersson, E., Schyberg,  
912 H., Culoma, A., Meynart, R., Endemann, M. and Ingmann, P., 2005: The Atmospheric Dynamics Mission for global  
913 wind field measurement. *Bull. Amer. Meteor. Soc.*, 86, 73–87  
914
- 917 Straume, A.-G., Rennie, M., Isaksen, L., de Kloe, J., Marseille, G.-J., Stoffelen, A., Flament, T., Stieglitz, H., Dabas,  
918 A., Huber, D., Reitebuch, O., Lemmerz, C., Lux, O., Marksteiner, U., Rahm, S., Weiler, F., Witschas, B., Meringer,  
919 M., Schmidt, K., Nikolaus, I., Geiss, A., Flamant, P., Kanitz, T., Wernham, D., von Bismark, J., Bley, S., Fehr, T.,  
920 Floberghagen, R., and Parrinello, T., 2019: ESA's Space-based Doppler Wind Lidar Mission Aeolus – First Wind and  
921 Aerosol Product Assessment Results, in: International Laser Radar Conference, Hefei, China, 24–28 June 2019.  
922
- 923 Sugimoto, N. and Lee, C. H., 2006: Characteristics of dust aerosols inferred from lidar depolarization measurements  
924 at two wavelengths, *Appl. Optics*, 45, 7468–7474  
925
- 926 Tan D. G. H., E. Andersson, J. De Kloe, G.-J. Marseille, A. Stoffelen, P. Poli, M.-L. Denneulin, A. Dabas, D. Huber,  
927 O. Reitebuch, P. Flamant, O. Le Rille, and H. Nett, 2008: The ADM-Aeolus wind retrieval algorithms, *Tellus A:*  
928 *Dynamic Meteorology and Oceanography*, 60:2, 191-205, DOI: [10.1111/j.1600-0870.2007.00285.x](https://doi.org/10.1111/j.1600-0870.2007.00285.x)  
929



- 930 Tucker, S. C., C. S. Weimer, S. Baidar, and R. M. Hardesty, 2018: The Optical Autocovariance Wind Lidar. Part I:  
931 OAWL Instrument Development and Demonstration. *J. Atmos. Oceanic Technol.*, **35**, 2079–  
932 2097, <https://doi.org/10.1175/JTECH-D-18-0024.1>.  
933
- 934 Turk, F. J., Hristova-Veleva, S., Durden, S. L., Tanelli, S., Sy, O., Emmitt, G. D., Greco, S., and Zhang, S. Q., 2020:  
935 Joint analysis of convective structure from the APR-2 precipitation radar and the DAWN Doppler wind lidar during  
936 the 2017 Convective Processes Experiment (CPEX), *Atmos. Meas. Tech.*, **13**, 4521–4537,  
937 <https://doi.org/10.5194/amt-13-4521-2020>  
938
- 939 Wang, Y., C. Williamson, G. Huynh, D. Emmitt, and S. Greco, 2012: Airborne Doppler wind lidar data fusion with  
940 a diagnostic wind model, *Proc. SPIE 8379, Laser Radar Technology and Applications XVII*, 83790L (14 May  
941 2012); <https://doi.org/10.1117/12.918466>  
942
- 943 Wirth, M., Fix, A., Mahnke, P., and Co-authors, 2009: The airborne multi-wavelength water vapor differential  
944 absorption lidar WALES: system design and performance. *Appl. Phys. B* **96**, 201 (2009).  
945 <https://doi.org/10.1007/s00340-009-3365-7>  
946
- 947 Witschas, B., S. Rahm, A. Dörnbrack, J. Wagner, and M. Rapp, 2017: Airborne Wind Lidar Measurements of Vertical  
948 and Horizontal Winds for the Investigation of Orographically Induced Gravity Waves. *J. Atmos. Oceanic Technol.*, **34**,  
949 1371–1386, <https://doi.org/10.1175/JTECH-D-17-0021.1>.  
950
- 951 Witschas, B., Lemmerz, C., Geiß, A., Lux, O., Marksteiner, U., Rahm, S., Reitebuch, O., and Weiler, F., 2020: First  
952 validation of Aeolus wind observations by airborne Doppler wind lidar measurements, *Atmos. Meas. Tech.*, **13**, 2381–  
953 2396, <https://doi.org/10.5194/amt-13-2381-2020>  
954
- 955 Wulfmeyer, V., R. M. Hardesty, D. D. Turner, A. Behrendt, M. P. Cadetdu, P. DiGirolamo, P. Schlüssel, J. Van Baelen,  
956 and F. Zus, 2015: A review of the remote sensing of lower tropospheric thermodynamic profiles and its indispensable



957 role for the understanding and the simulation of water and energy cycles, *Rev. Geophys.*, 53,819–895,

958 doi:10.1002/2014RG000476

959

960 Zhang, J. A., Atlas, R., Emmitt, G. D., Bucci, L., & Ryan, K., 2018: Airborne doppler wind lidar observations of the

961 tropical cyclone boundary layer. *Remote Sensing*, 10(6). <https://doi.org/10.3390/rs10060825>

962

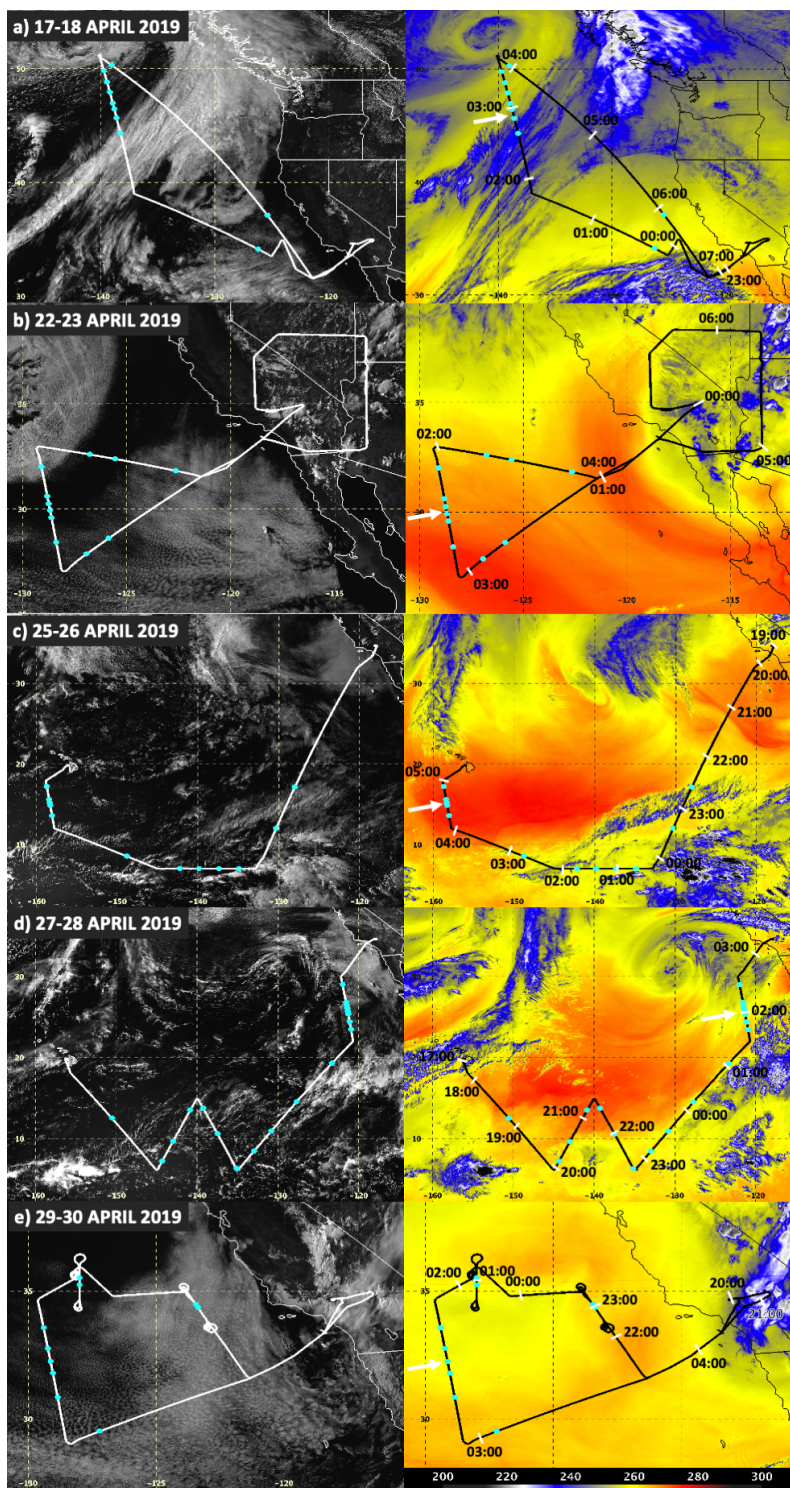
963



<b>Flight Date</b>	<b>DAWN Operating Mode</b>
17-18 April 2019	Stare at 90 degree azimuth, 20 pulse integration (1.2 UTC to 3.7 UTC, 0.5 km/profile) 5 azimuths, 20 pulses/azimuth (sporadically from 2.5 to 3.7 UTC, 4 km/profile) 5 azimuths, 40 pulses/azimuth (3.7 to 7.7 UTC, 8 km/profile)
22-23 April 2019	5 azimuths, 20 pulses/azimuth
25-26 April 2019	2 azimuths, 200 pulses/azimuth (22.4 to 23.6 UTC, 9 km/profile) 5 azimuths, 20 pulses/azimuth
27-28 April 2019	5 azimuths, 20 pulses/azimuth
29-30 April 2019	5 azimuths, 20 pulses/azimuth

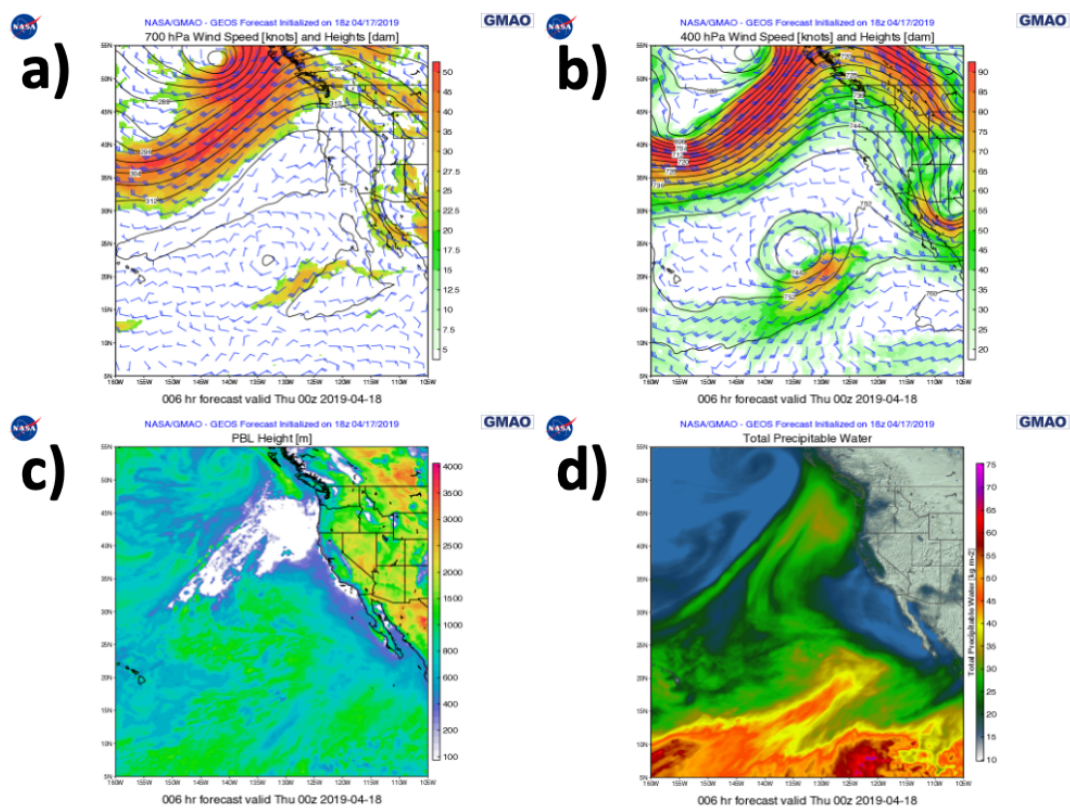
**Table 1:** A listing of DAWN operating mode throughout the five flights of the campaign and the approximate spacing between profiles.

964  
 965  
 966  
 967  
 968  
 969  
 970  
 971  
 972  
 973  
 974  
 975  
 976  
 977  
 978



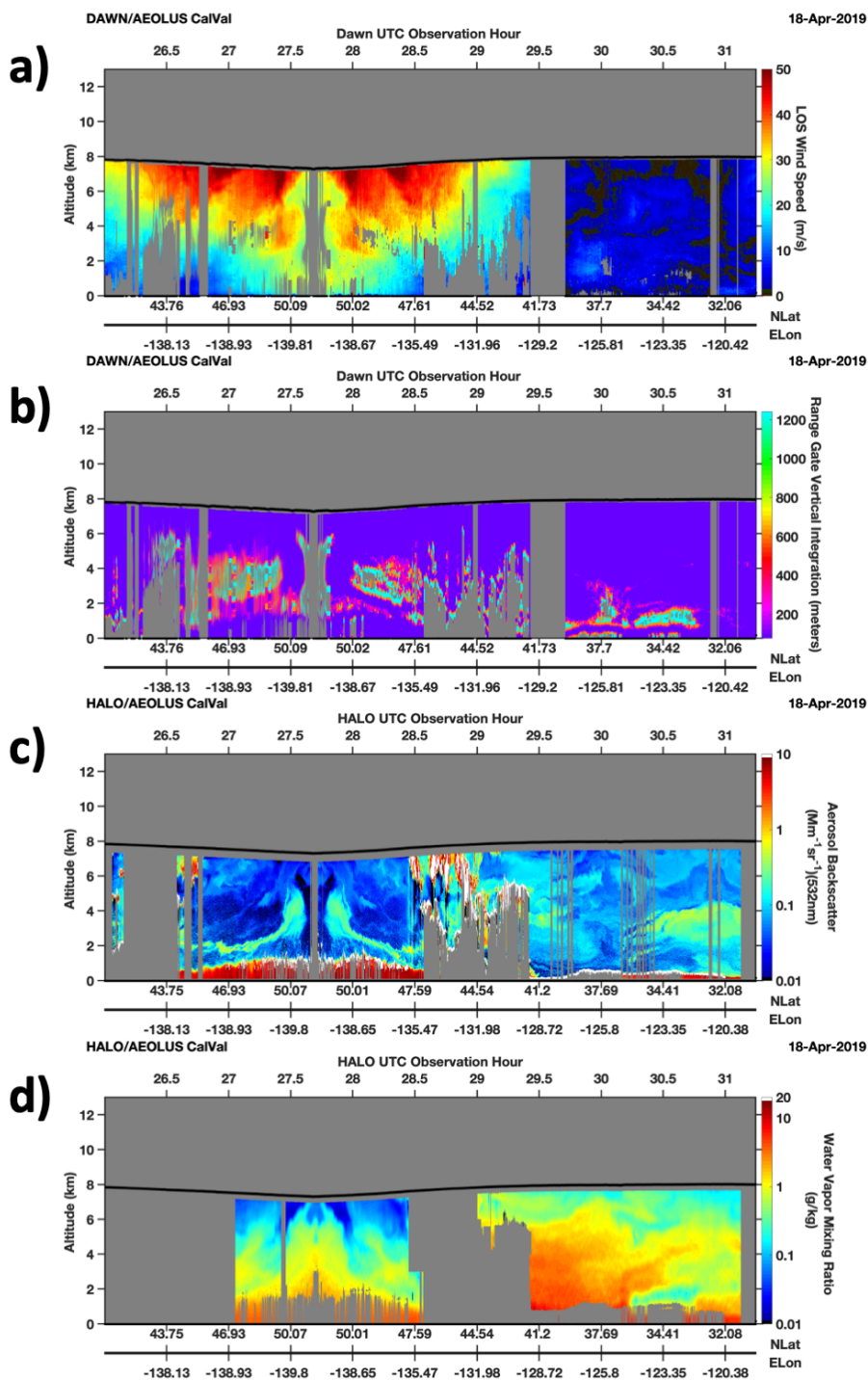


980  
981 **Figure 1: DC-8 flight track (bold lines) overlaid atop GOES-17 0.64  $\mu\text{m}$  visible (left) and 7.3  $\mu\text{m}$  water vapor**  
982 **brightness temperature (right, in degrees Kelvin) at (a) 00 UTC on 18 April, (b) 00 UTC on 23 April, (c) 0030**  
983 **UTC on 26 April, (d) 2230 UTC on 27 April, and (e) 00 UTC on 30 April. DC-8 aircraft position at hourly**  
984 **intervals is annotated on the right panels. Cyan circles indicate where dropsondes were released. White**  
985 **arrows point to straight northwest-southeast oriented segments where the DC-8 under flew the Aeolus laser**  
986 **track at a 6 km altitude, for durations ranging from ~45 to 110 minutes.**



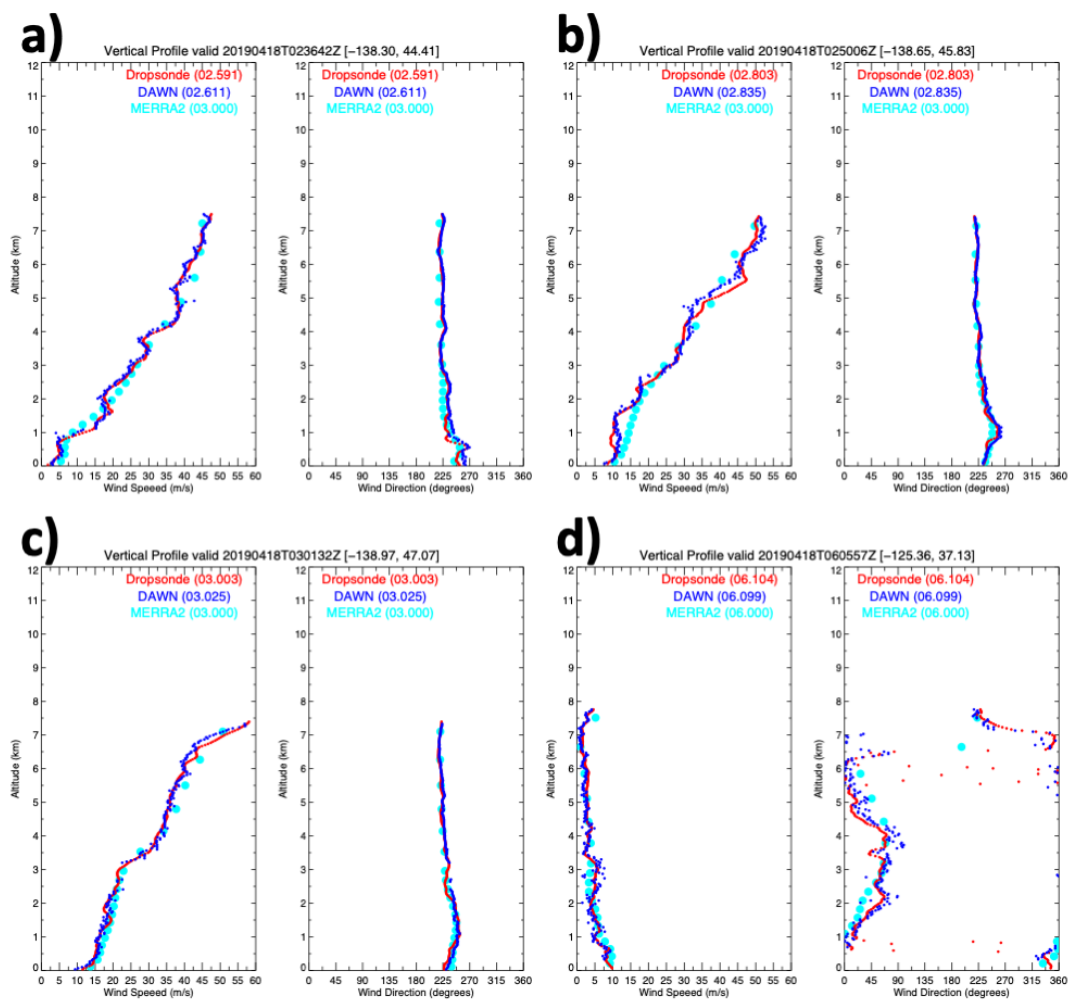
987  
988  
989  
990  
991  
992  
993

Figure 2: NASA GMAO GEOS-5 6-hour forecast of (a) 700 hPa wind, (b) 400 hPa wind, (c) PBL height, and (d) total precipitable water, valid at 00 UTC on 18 April 2019.





995 **Figure 3: (a) The absolute value of the DAWN horizontal line of sight (HLOS) wind speed measurement, projected 90° to**  
996 **the right of the aircraft heading from 0200 to 0715 UTC (i.e. 26.00-31.25 above) on 18 April 2019. The bold black line atop**  
997 **the colored cross section indicates DC-8 flight altitude. (b) The depth of vertical signal integration required to achieve**  
998 **sufficient signal for a DAWN wind retrieval. (c) HALO 532 nm aerosol backscatter coefficient, shown with a logarithmic**  
999 **color scale to accentuate variations in the free troposphere aerosol distributions. (d) HALO water vapor mixing ratio also**  
1000 **shown with a logarithmic color scale. Grey areas in the DAWN and HALO cross sections indicate aircraft turns (roll  $\geq$**   
1001 **2.5°), areas beneath opaque cloud cover, inadequate signal return inhibiting retrieval at a particular altitude, or**  
1002 **instrument downtime.**  
1003  
1004



1005

1006 **Figure 4: Dropsonde (red), DAWN (blue), and MERRA-2 (cyan) for DAWN profiles at (a) 0236, (b) 0250, (c) 0301, and**  
1007 **(d) 0605 UTC on 18 April 2019.**

1008

1009

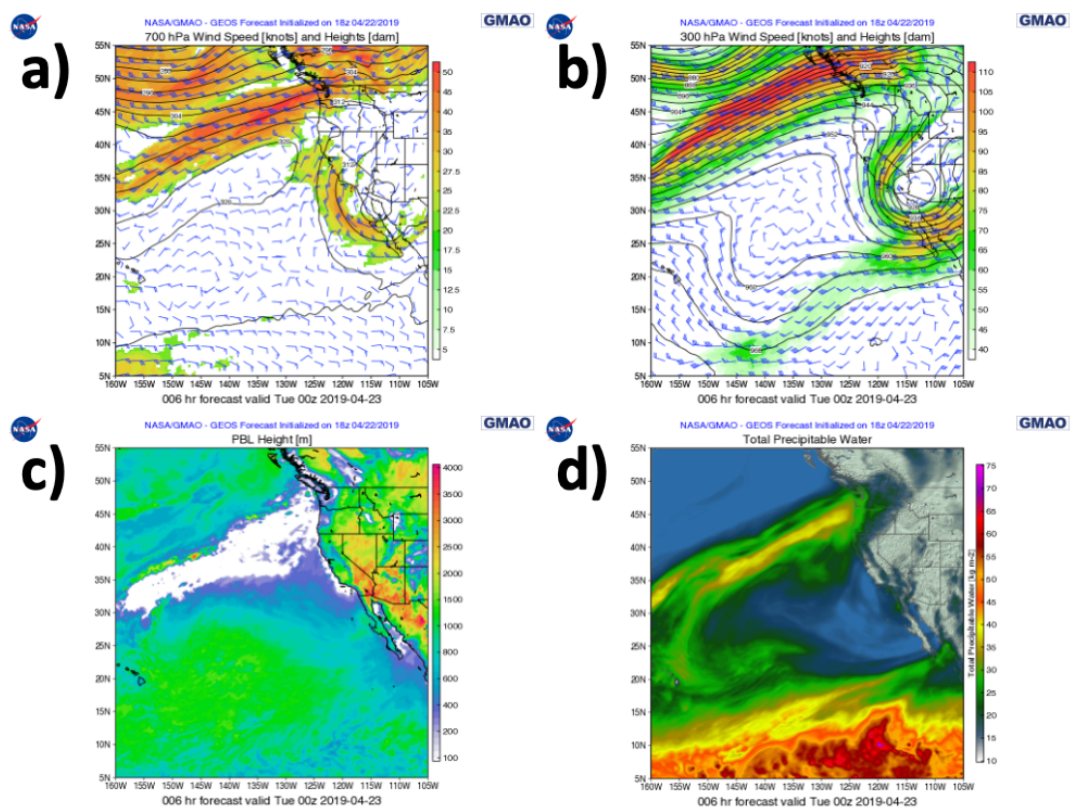
1010

1011

1012

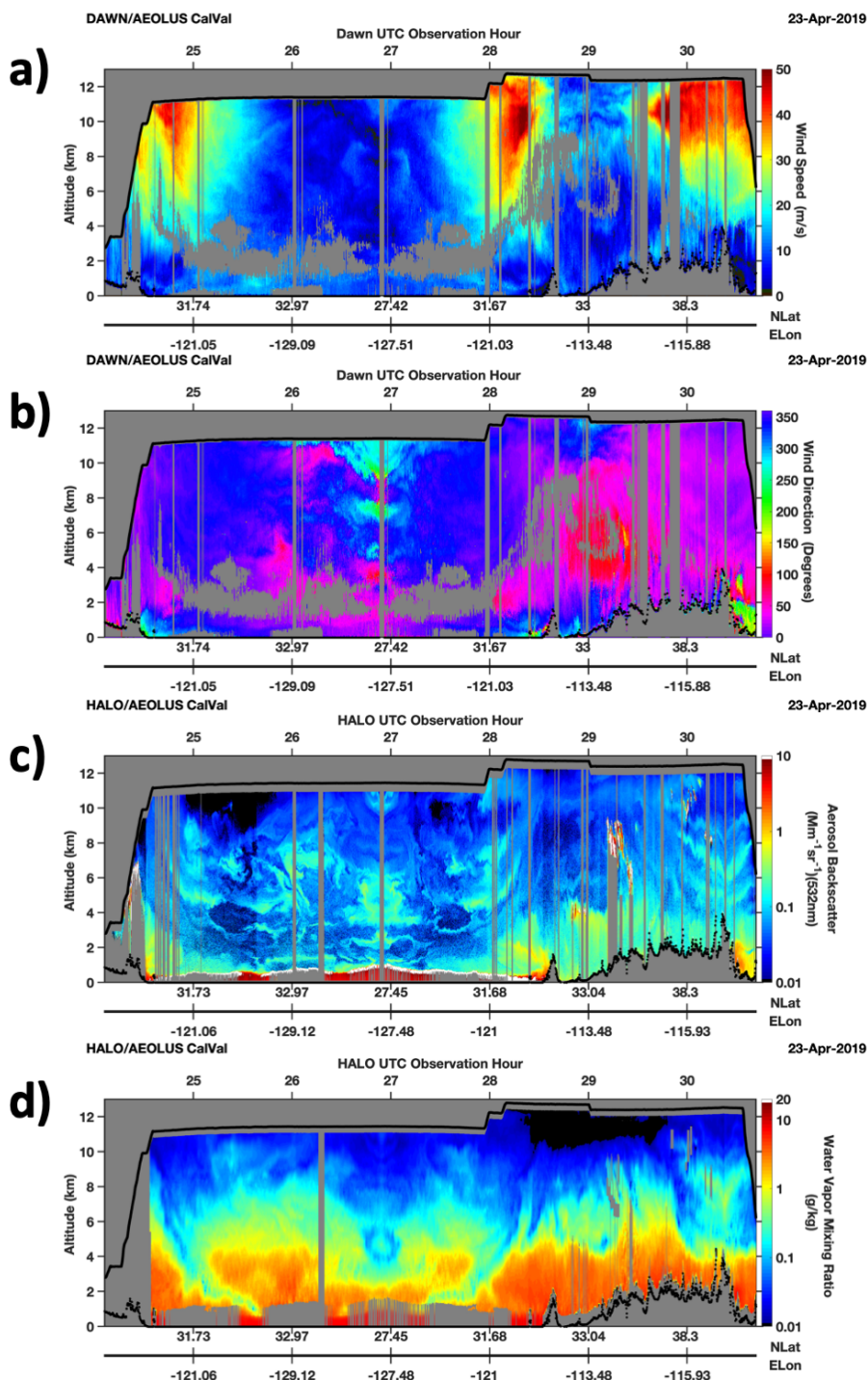
1013

1014



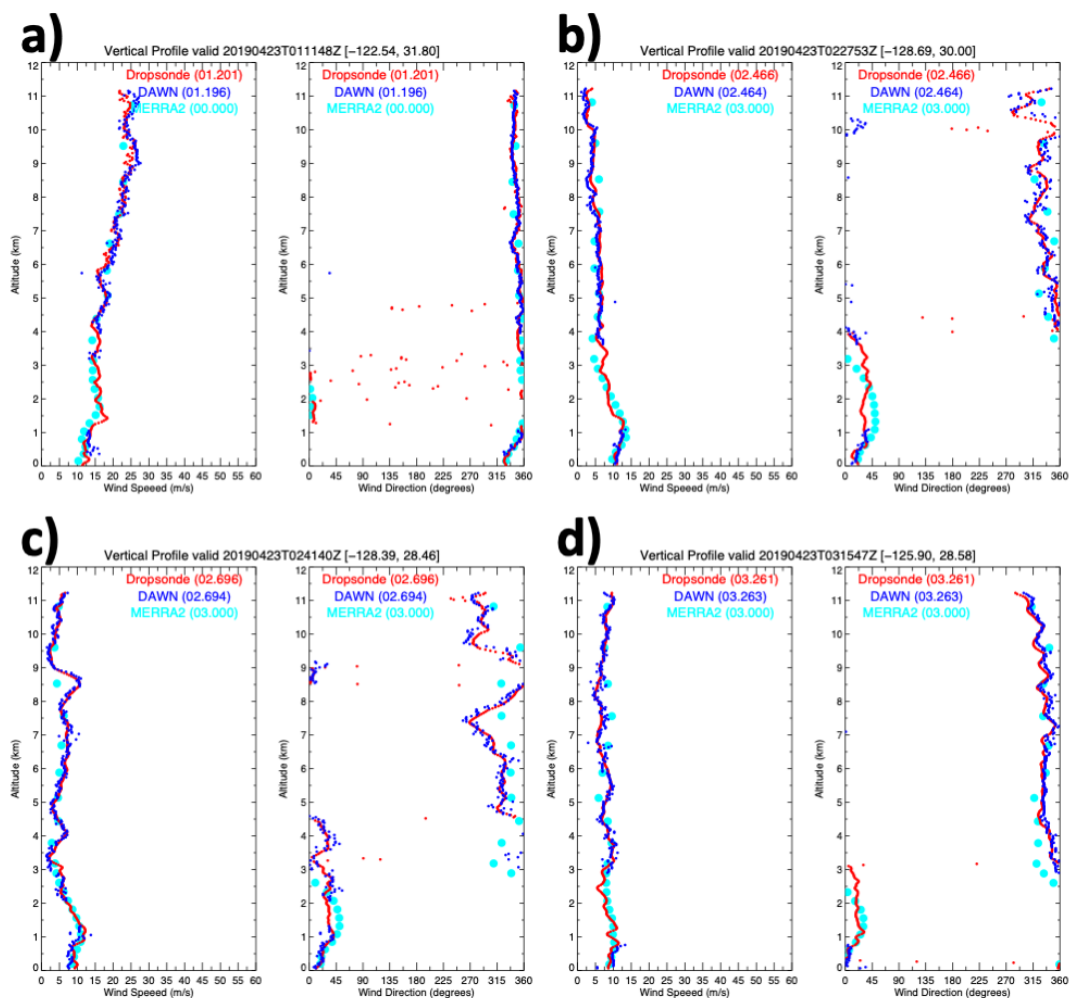
1015  
1016 **Figure 5: NASA GMAO GEOS-5 6-hour forecast of (a) 700 hPa wind, (b) 300 hPa wind, (lower-left) PBL height, and**  
1017 **(lower-right) total precipitable water, valid at 00 UTC on 23 April 2019.**

1018  
1019



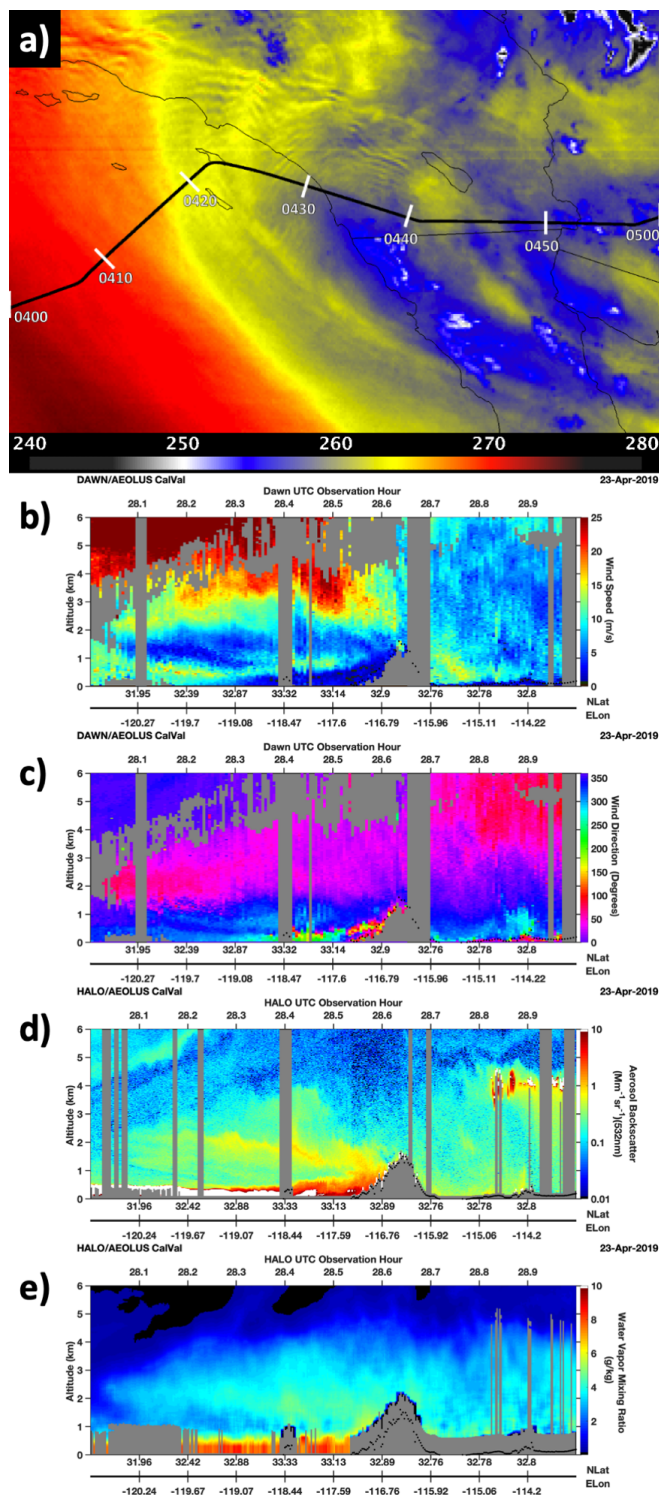


1021 **Figure 6: (a-b) DAWN wind speed and direction for the 22-23 April 2019 flight. © HALO 532 nm aerosol backscatter. (d)**  
1022 **HALO water vapor mixing ratio.**  
1023



1024  
1025  
1026  
1027

Figure 7: Dropsonde (red), DAWN (blue), and MERRA-2 (cyan) for DAWN profiles at (a) 0111 , (b) 0227, (c) 0241, and (d) 0315 UTC on 23 April 2019.





1029 **Figure 8: (a) GOES 7.3  $\mu\text{m}$  water vapor brightness temperature (in degrees Kelvin) at 0426 UTC on 23 April 2019. The**  
1030 **color scale of this image (bottom) has been compressed relative to that shown in Figure 1 to accentuate mountain wave**  
1031 **patterns along flight track (bold black line). (b-c) DAWN wind speed and direction along the one-hour flight period**  
1032 **shown in the GOES image. The wind speed color scale has also been compressed to accentuate wind speed variations**  
1033 **associated with the mountain waves. (d) HALO 532 nm aerosol backscatter. (e) HALO water vapor mixing ratio,**  
1034 **colorized with a linear scale to accentuate details.**  
1035

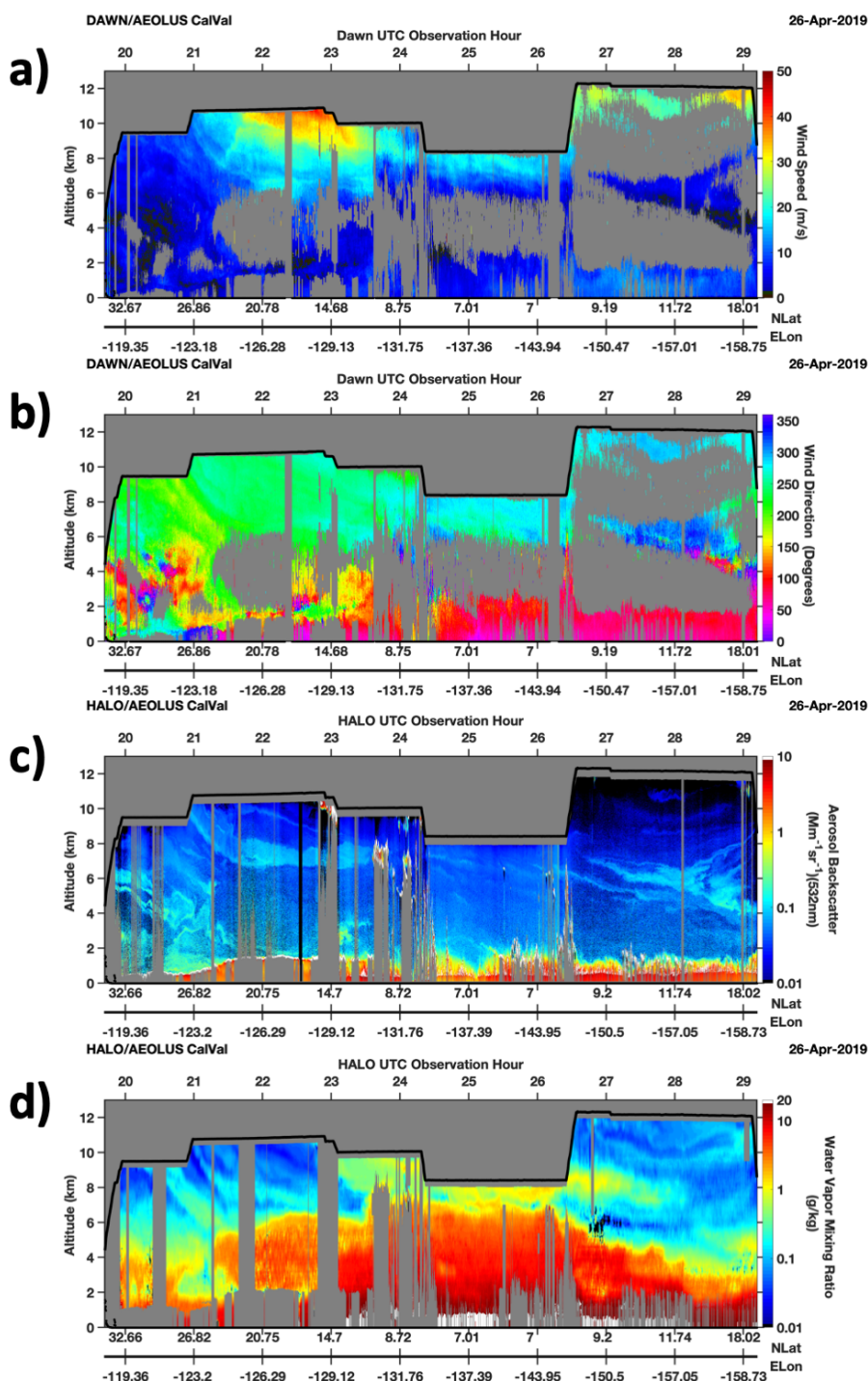
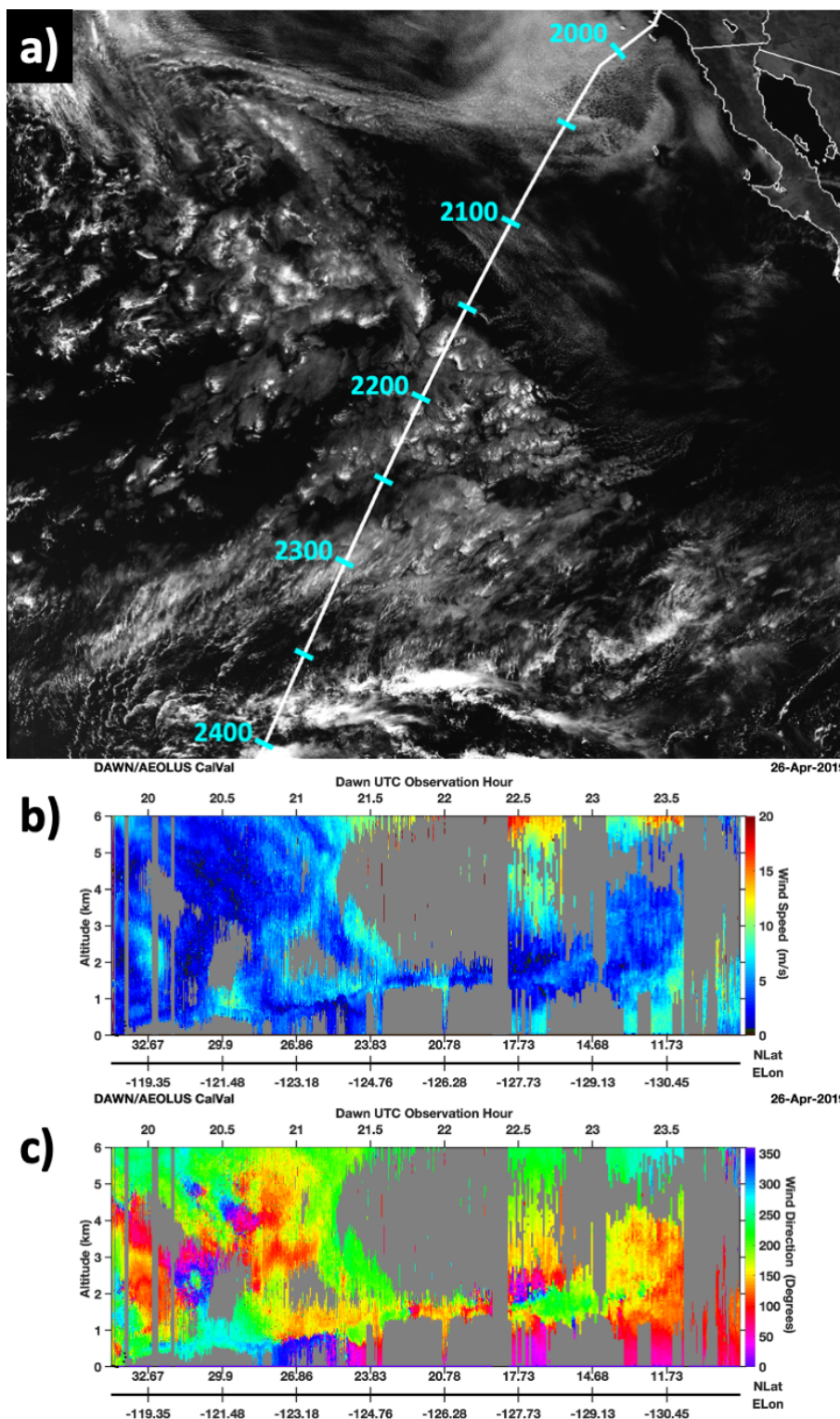
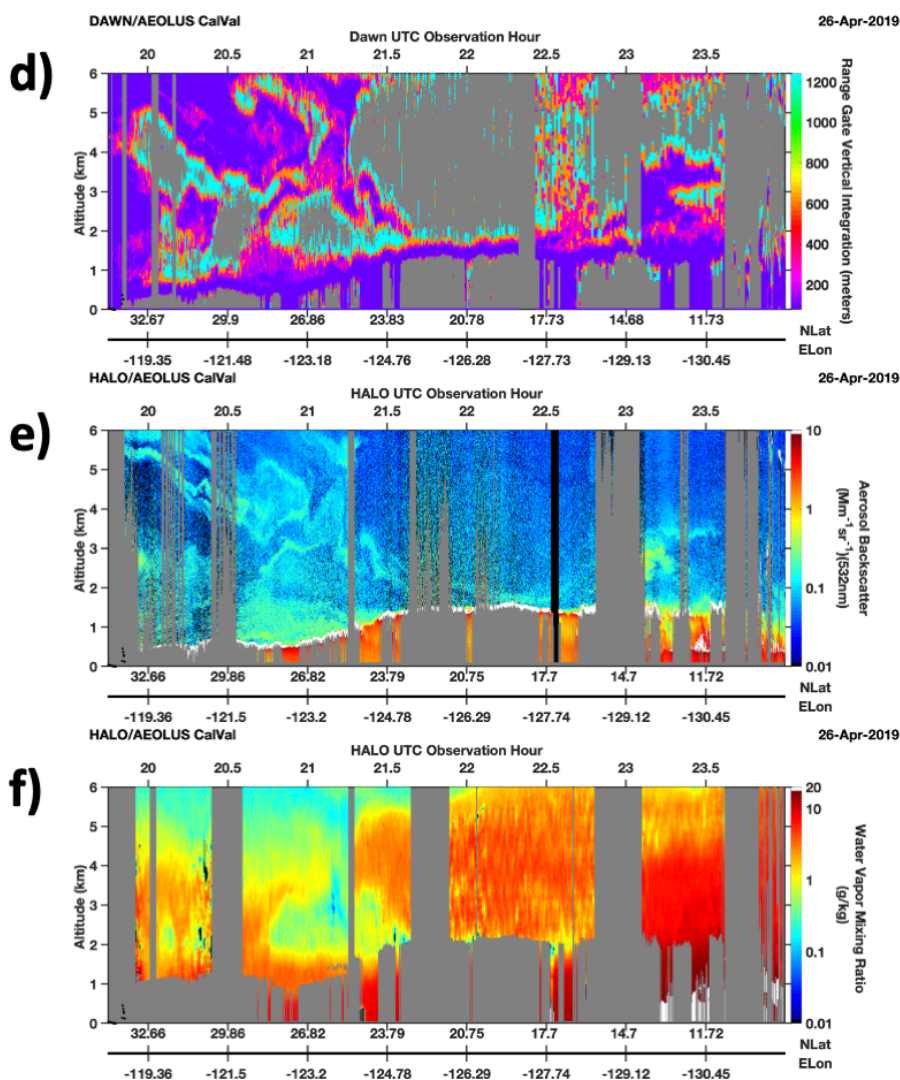


Figure 9: The same as Figure 6 except for the 25-26 April 2019 flight.

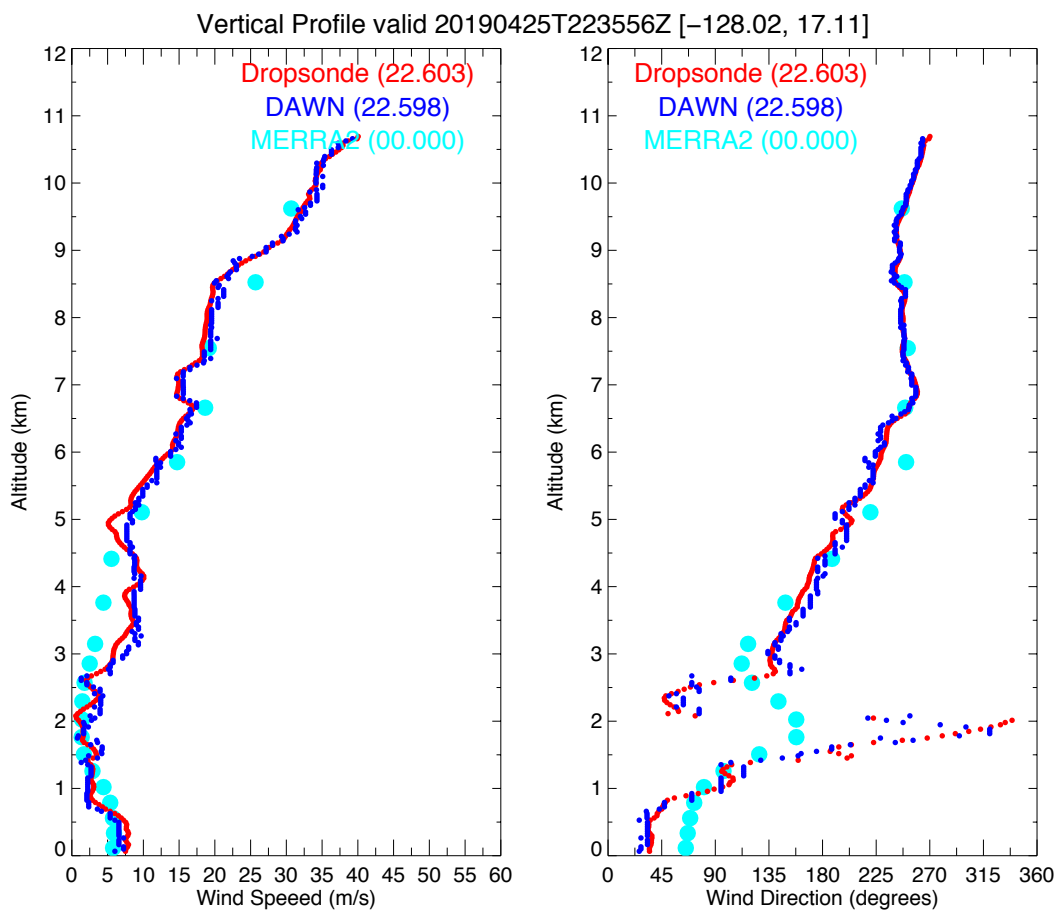
1036  
1037  
1038





1040

1041 Figure 10: (a) GOES-17 0.64  $\mu\text{m}$  visible at 2200 UTC on 25 April 2019 overlaid with a nearly four-hour duration DC-8  
1042 flight track over stratocumulus and tropical convection. (b-c) DAWN wind speed and direction. DAWN wind speed color  
1043 scale was compressed to 0-20 m/s to accentuate wind speed variations along flight track. Only data between 0 and 6 km  
1044 altitude are shown (d) The depth of vertical signal integration required to achieve sufficient signal for a DAWN wind  
1045 retrieval. (e-f) HALO 532 nm aerosol backscatter and water vapor mixing ratio.



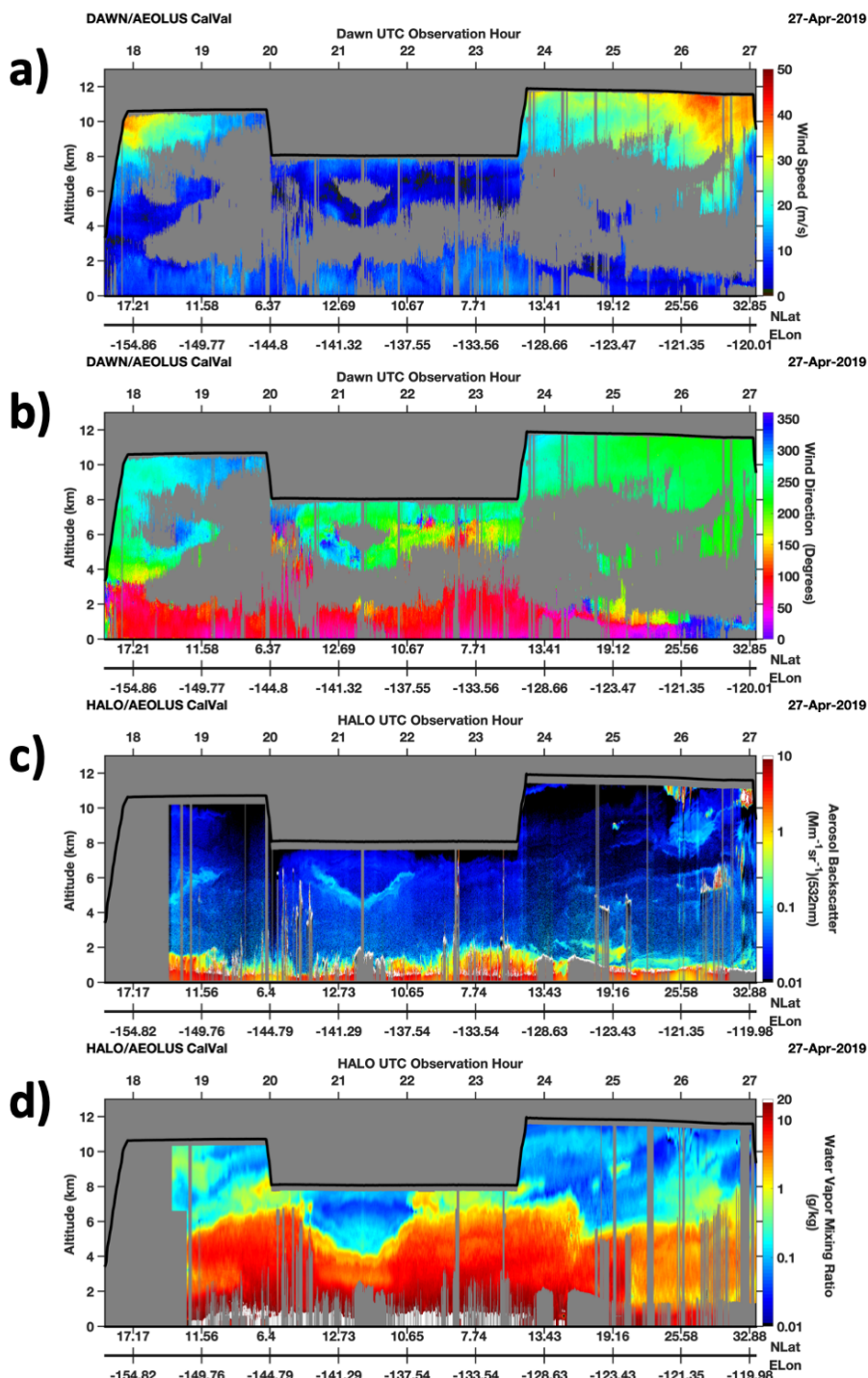
1046

1047 **Figure 11: Dropsonde (red), DAWN (blue), and MERRA-2 (cyan) for DAWN profiles at 2235 UTC on 25 April 2019, in**  
1048 **an air mass with weak aerosol signal within the 2-6 km altitude layer when DAWN was operating in 2-azimuth, 200**  
1049 **pulse/azimuth mode.**

1050

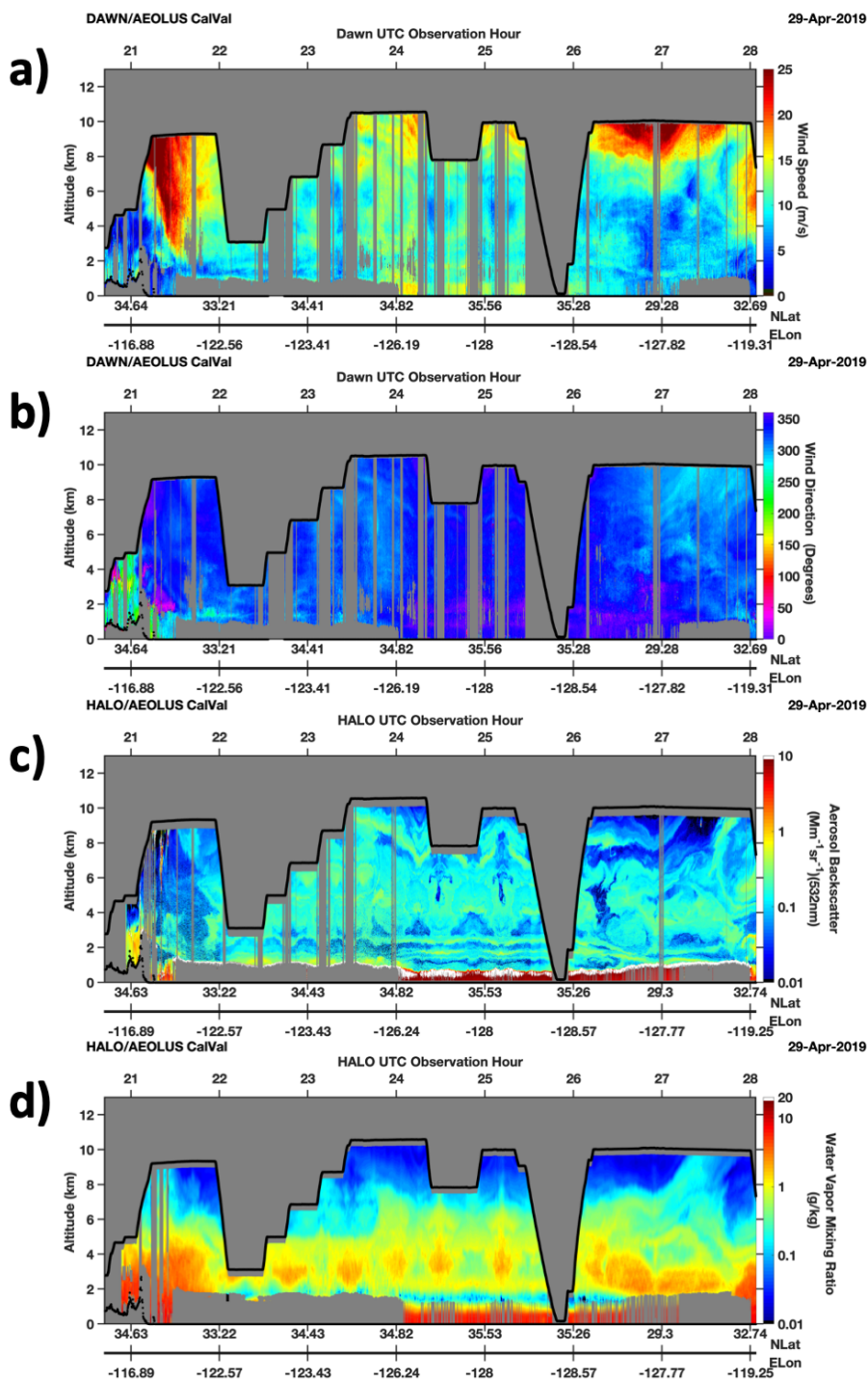
1051

1052



1053  
1054

Figure 12: The same as Figure 6 except for the 27-28 April 2019 flight.

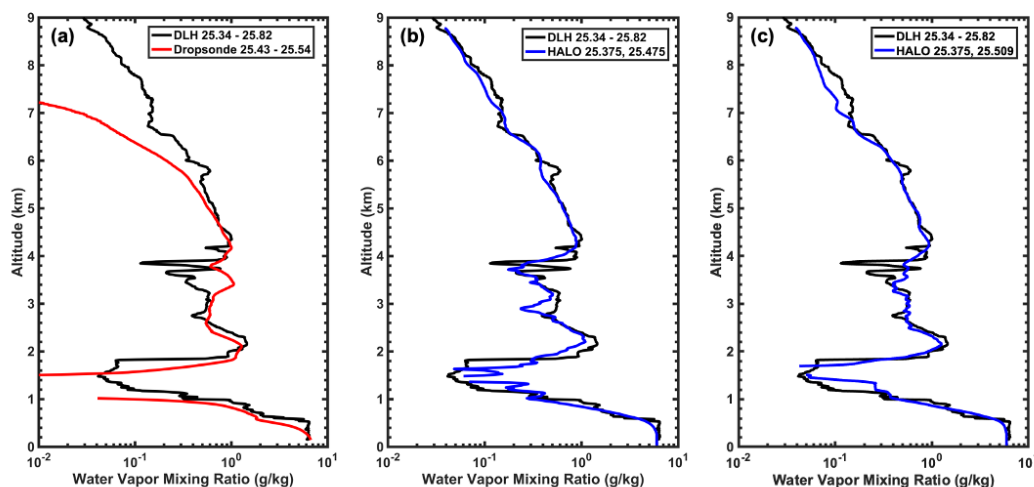




1056 **Figure 13: The same as Figure 6 except for the 29-30 April 2019 flight. The color scale of the DAWN wind speed is**  
1057 **compressed to 0 to 25 m/s to accentuate the lower wind speeds observed during this flight.**



1058



1059

1060

1061

1062

1063

1064

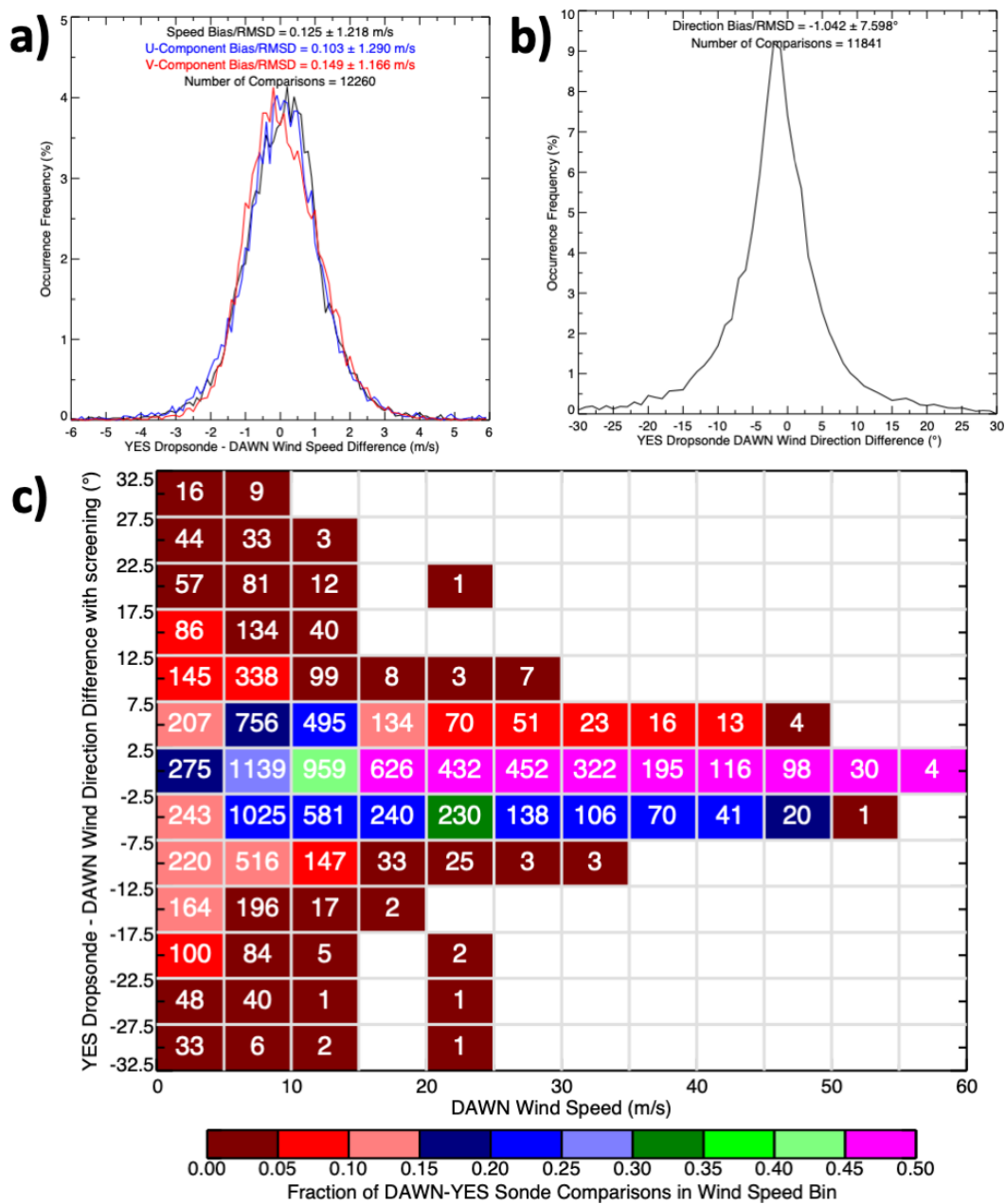
1065

1066

1067

1068

Figure 14: HALO and dropsonde comparisons with DLH. a) Yankee XDD dropsonde (red) comparison against DLH-derived water vapor mixing ratio profile (black) from the descending DC-8 spiral. The time of flight for the sonde and those also used to generate the DLH profile are indicated in the legend. b) HALO 315 m vertical and 12 km horizontal resolution WV profile (blue) comparison against DLH. Two HALO profiles are spliced together using the times indicated in the legend to account for the heterogeneity in the WV field over the spiral location as well as to account for the spatial offset between the HALO and DLH in situ spiral. c) same as b) but with a different profile chosen for the lower tropospheric splice region. Data are shown on a logarithmic scale to highlight the large dynamic range throughout the depth of the profile.

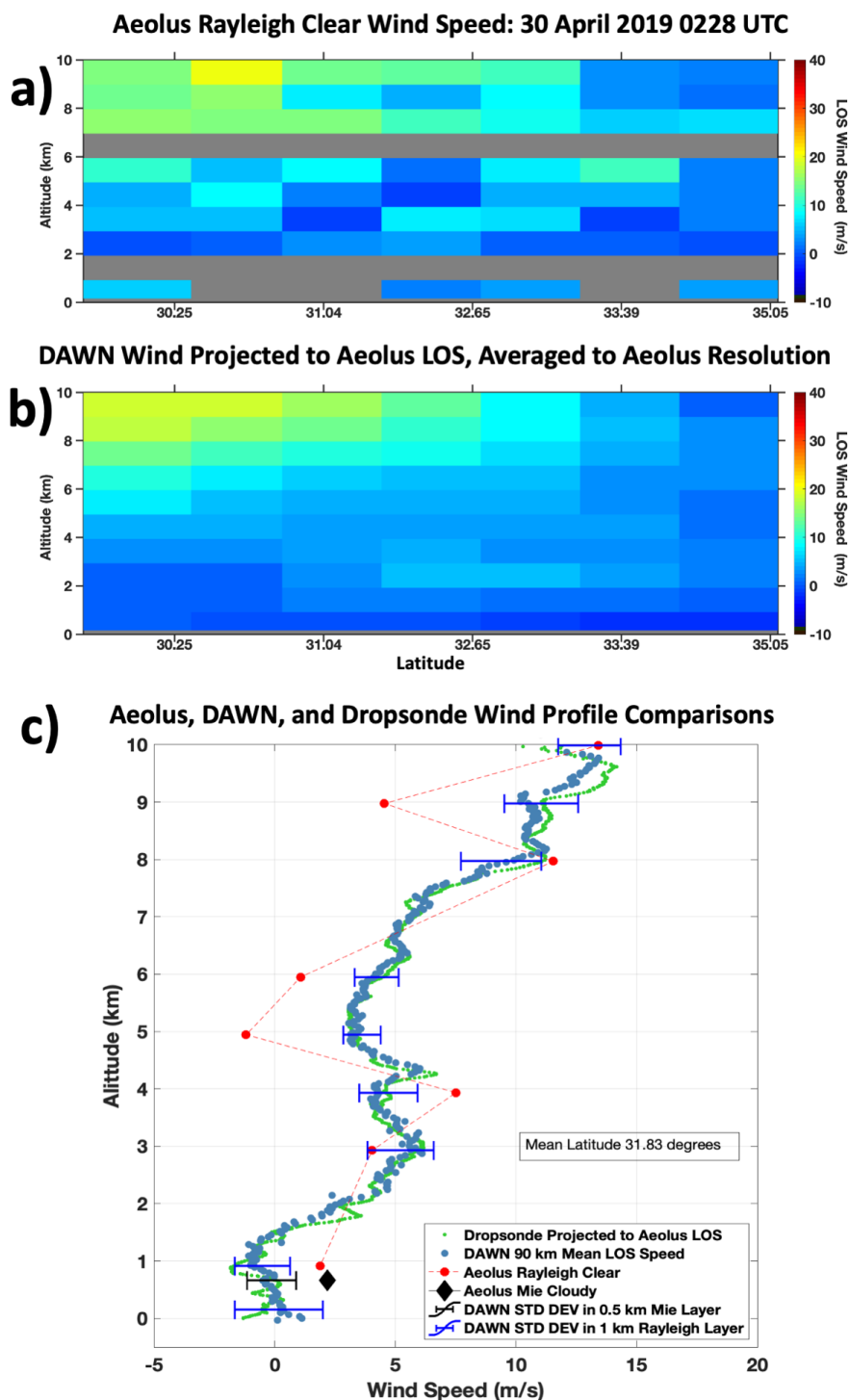


1069

1070 Figure 15: A comparison of DAWN and dropsonde vector wind speed (black), and u- and v-component speed (blue and  
 1071 red respectively, panel a) and direction (panel b) aggregated across all vertical bins with a valid DAWN retrieval, using  
 1072 the methods described in Section 2.3 (panel c) DAWN-sonde wind direction difference as a function of wind speed,

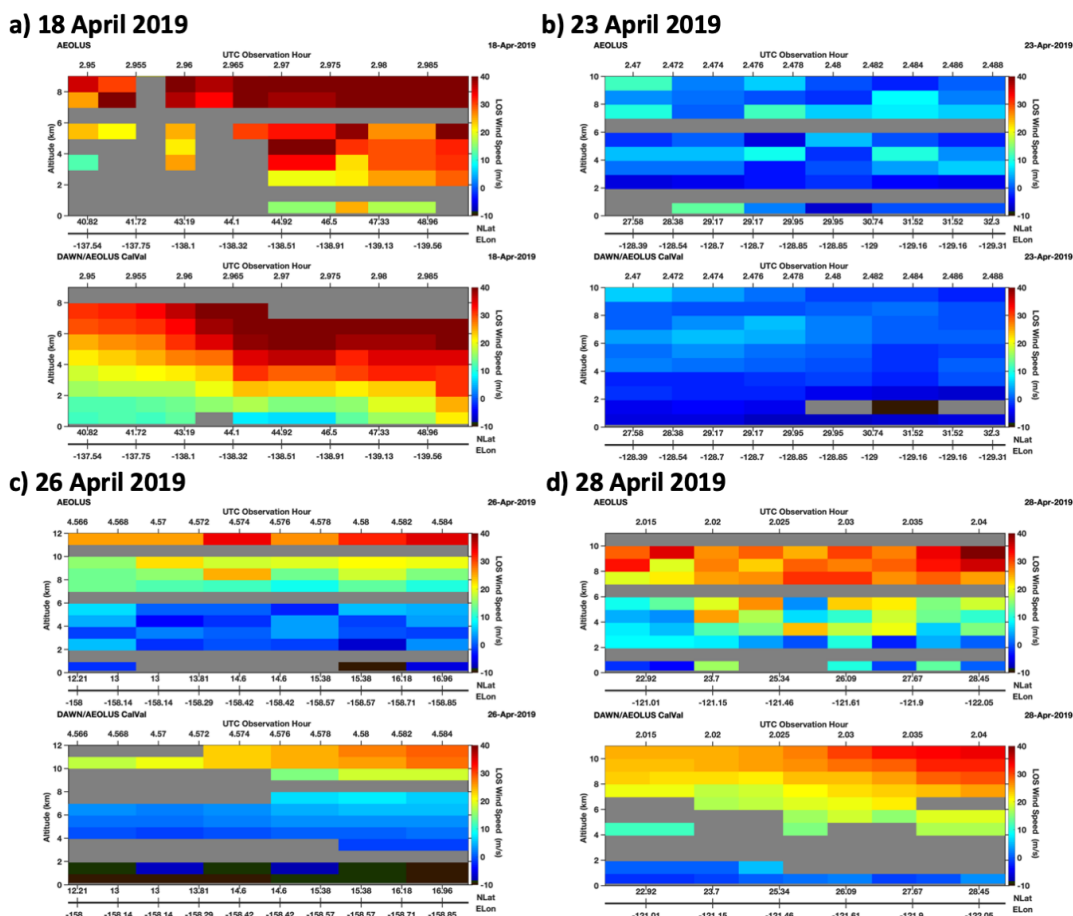


1073 clustered into 5° and 5 m/s bins. Bins are colored by the fraction of observations within a bin relative to the total samples  
1074 in each column. The number of samples is listed within each bin.  
1075





1077 **Figure 16: a) Aeolus Rayleigh clear and b) DAWN HLOS wind speed profile cross section, coinciding with the 0228 UTC**  
1078 **Aeolus overpass on 30 April 2019. c) The mean DAWN HLOS speed aggregated across the 90-km Rayleigh clear**  
1079 **integration distance (blue), dropsonde projected LOS speed (green), and Aeolus Rayleigh Clear (red) and Mie Cloudy**  
1080 **(black diamond) speed. DAWN variance across the Rayleigh vertical bin depth and ~90-km horizontal distance are also**  
1081 **overlaid with blue whiskers.**  
1082



1083

1084

1085

1086

1087

1088

1089

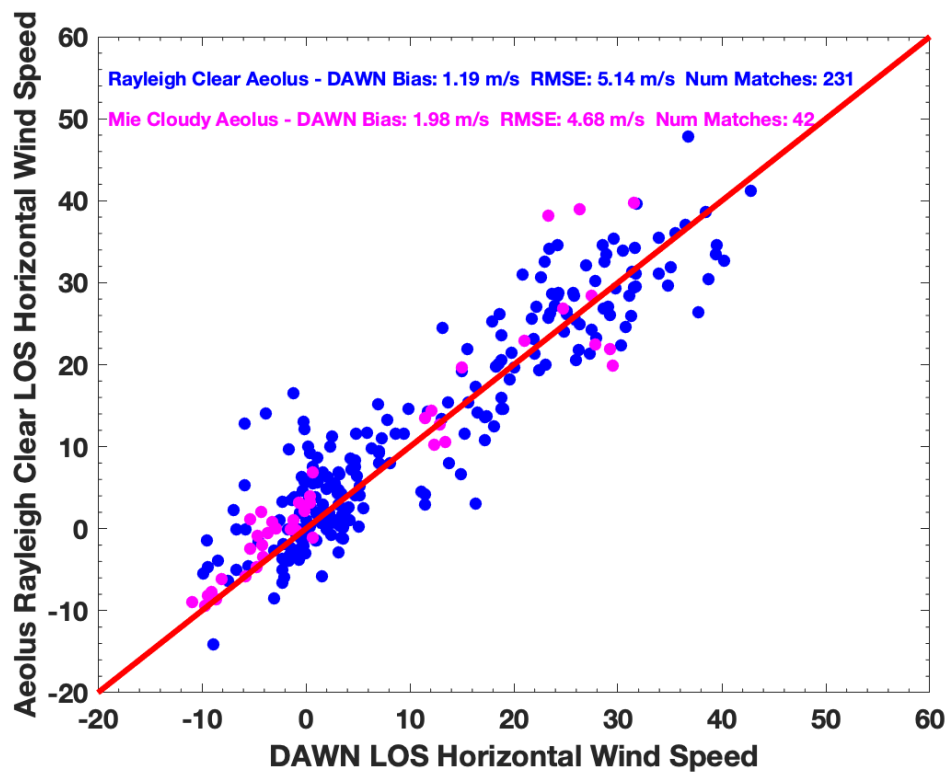
1090

1091

1092

1093

Figure 17: Aeolus Rayleigh clear (top) and the mean DAWN HLOS speed aggregated across 90-km Rayleigh clear integration distances (bottom), analogous to Figure 16a-b, for the four remaining Aeolus under-flights.



1094

1095 Figure 18: Aeolus-DAWN HLOS wind comparison based on 244 Aeolus Rayleigh clear (blue) and 43 Mie cloudy  
1096 (magenta) vertical bins aggregated across 46 profiles.

1097

1098